

Deep Learning Model for Inverse Design of Semiconductor Heterostructures with Desired Electronic Band Structures

Artem K Pimachev¹ and Sanghamitra Neogi^{1, *}

¹*Ann and H.J. Smead Aerospace Engineering Sciences,
University of Colorado Boulder, Boulder, Colorado 80303, USA*

Email: sanghamitra.neogi@colorado.edu

(Dated: February 8, 2023)

First-principles modeling techniques have shown remarkable success in predicting electronic band structures of materials. However, the computational costs make it challenging to use them for predicting band structures of semiconductor heterostructures, that show high variability of atomic structures. We propose a machine learning-assisted first-principles framework that bypasses expensive computations and predicts band structures from the knowledge of atomic structural features. Additionally, the framework directly connects modeling results and experimental data. For example, it accepts images obtained with angle-resolved photoemission spectroscopy as input and predicts the corresponding atomic structures. The framework leverages the physical relationship between atomic environments and bands. We demonstrate the framework using silicon/germanium based superlattices and heterostructures. Once trained on silicon-based systems, the framework can even predict band structures of gallium arsenide thin films. The physics-informed framework establishes an approach to expedite the design and discovery of complex materials with desired band structures, going beyond combinatorial approaches.

Semiconductor heterostructures are important condensed matter systems, both for fundamental research as well as for device applications [1]. Exploiting the full potential of these systems requires a complete understanding of their electronic band structures. The band structures dictate the physical response of the materials to external fields and determine their electrical, magnetic and optical properties. The electronic bands of layered materials or heterostructures are strongly affected by the variations of atomic structures, caused by the fabrication processes. Even in heterostructures grown with state-of-the-art nanofabrication techniques, the presence of various imperfections becomes unavoidable [2–4]. The imperfections strongly influence the structural order. The heterostructure may inherit approximate structural order of separate layers or exhibit a mixed character. First-principles modeling techniques, such as density functional theory (DFT), have shown remarkable success in predicting electronic properties of materials. Electronic bands of heterostructures are calculated using supercells that are chosen to be as large as is feasible to represent the structural order. Due to the varied structural order, the supercell bands may resemble the Bloch states of either, or both of the layers. Different unfolding algorithms [5–10] have successfully identified the Bloch character of supercell bands, especially for alloys [11, 12]. However, the high computational costs make it challenging to analyze all possible heterostructures using first-principles techniques. A first-principles approach to predict and design band structures of heterostructures has not been established. As a result, combinatorial approaches are being pursued to design heterostructures that exhibit desired electronic properties. The key questions remain: what Bloch character do bands of fabri-

cated heterostructures exhibit? how closely do they correspond to the bands of constituting materials? and how can one design heterostructures that exhibits bands with desired characters?

In this article, we present a first-principles modeling framework to expedite the prediction and design of band structures of semiconductor heterostructures. The framework is assisted by machine learning (ML) techniques and establishes a relationship between atomic structural environments and electronic bands. Physical principles are increasingly being incorporated in ML-based approaches to accelerate prediction of materials properties [13]. A recent study showed that awareness of structural motifs enables ML model to accurately predict bandgaps of metal oxides [14]. Our previous ML model exploited the relationship between local structures and global electronic properties of semiconductor structures. The model successfully predicted electronic transport properties of experimental heterostructures [15]. The present framework reveals the Bloch character of the heterostructure bands. Additionally, the framework directly connects first-principles modeling and experiments. For example, our framework can accept images from angle-resolved photoemission spectroscopy (ARPES) as input and predict the atomic structures of the corresponding systems. The atomic structures could be compared with structural characterization data. The comparison not only will demonstrate the model performance but identify structural features that result in desired band structures. Our framework thus facilitates the inverse design of semiconductor heterostructures with desired electronic properties.

We implement the framework using two ML models: (1) *a forward learning model* that accepts atomic struc-

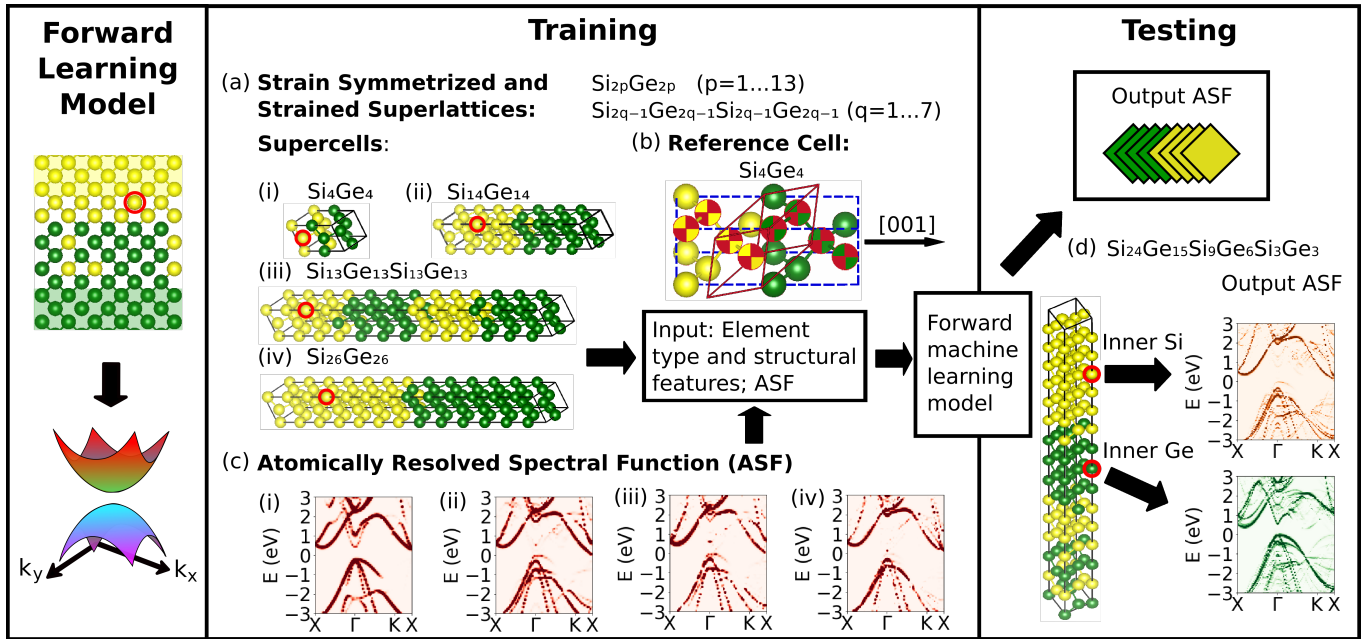


FIG. 1. **Outline of forward ML model:** (a) Training strain-symmetrized and strained superlattices with various periods and compositions. Representative supercells of (i) Si_4Ge_4 , (ii) $\text{Si}_{14}\text{Ge}_{14}$, (iii) $\text{Si}_{13}\text{Ge}_{13}\text{Si}_{13}\text{Ge}_{13}$ and (iv) $\text{Si}_{26}\text{Ge}_{26}$ superlattices. (b) Representative reference cell to obtain unfolded spectral functions (SF). Two types of descriptors are used: Element type and structural features. (c)(i)-(iv) Property value corresponding to descriptors: atomically resolved SFs (ASFs) of atoms marked with red circles in supercells shown in (a). (d) Trained ML models are tasked to predict ASFs of atoms in heterostructure, $\text{Si}_{24}\text{Ge}_{15}\text{Si}_9\text{Ge}_6\text{Si}_3\text{Ge}_3$. Predicted ASFs are compared with DFT results.

tural features as input and predicts the electronic bands of the corresponding heterostructure, and (2) *a reverse learning model* that accepts computed DFT band structures or measured ARPES spectra as input and predicts the atomic structural features of the corresponding system. We demonstrate the framework using a class of silicon (Si)/germanium (Ge) superlattices and heterostructures. Both superlattice and heterostructure configurations are periodically extended. Within one period of a model configuration, a superlattice includes one Si and one Ge layer while a heterostructure includes multiple Si and Ge layers of varied thicknesses. Silicon-based structures are chosen because of their wide use in technological applications and the ease of fabrication. However, our approach is applicable to other materials. For example, the framework can predict the relationship between ARPES spectra and atomic structures present in gallium arsenide (GaAs) thin film samples.

FORWARD LEARNING MODEL

Figure 1 shows the outline of our forward learning model. We consider Si/Ge superlattices with different periods and compositions as training structures. The structures are chosen such that the trained model could guide design of diverse heterostructures for various ap-

plications. We identify a set of features to describe the environments, $CN(\mathbf{r}_p)$, for each atom of a superlattice or heterostructure. Here, $CN(\mathbf{r}_p)$ refers to the local atomic configuration associated with atom p , located at position \mathbf{r}_p . We compute the effective band structures (EBS) or spectral functions (SF) for each atom, using DFT. These atomically resolved band structures (AEBS) or spectral functions (ASF) vary significantly with the changes of the atomic environment. We hypothesize that a direct relationship exists between environment features and corresponding ASFs, and train the forward model accordingly. The trained model accepts environment descriptors for atoms in test superlattices or heterostructures as input, and predicts the associated ASFs. Thus, the components of the forward learning model are as follows: (1) formulation of descriptors of $CN(\mathbf{r}_p)$, (2) generation of ASF training data, (3) implementation of ML models to identify descriptor-ASF relationships, and, (4) comparison of ML predictions for new structures with DFT results.

(1) Formulation of Atomic Environment Descriptors

In Fig. 1(a, b), we show representative configurations of training Si_nGe_n superlattices. Here, the subscript n refers to the number of Si and Ge monolayers. We list all training and test structures investigated in this ar-

TABLE 1. Summary of Data Used in the Proposed Machine Learning Framework

Structure Type	Training Structures	Input Features	Input Properties	Test Structures
Forward Learning Model: Neural Network (NN) & Random Forests (RF) Model				
Strain-symmetrized and strained SLs	$\text{Si}_{2p}\text{Ge}_{2p}$ $(p = 1, 2, \dots, 13)$ $(\text{Si}_{2q-1}\text{Ge}_{2q-1})^2$ $(q = 1, 2, \dots, 7)$ • 5 applied strains: [0.00%, 0.59%, 1.16%, 1.73%, 2.31%] • Total: 120 structures • Atomic environments: $6 \times 4 \times \left(\sum_{i=1}^{13} p_i + \sum_{j=1}^7 (2q_j - 1) \right) = 3360$	• Atom type: 1 feature/atom • Effective bond lengths, b_x & b_z : 2 features/atom • Order parameters, $Q_{x,z}^{1,2,3}$: 6 features/atom • Total: 9×3360 features	• Spectral weights, $A^p(k, E)$: $k \times E = 64 \times 96$ per atom (p) • Total: $64 \times 96 \times 3360$	• HS: $\text{Si}_{24}\text{Ge}_{15}\text{Si}_9\text{Ge}_6\text{Si}_3\text{Ge}_3$ 60 atoms Input features: 9×60 Output weights: $64 \times 96 \times 60$ • SL: $\text{Si}_{28}\text{Ge}_{28}$ (see SI Figure 2) 56 atoms Input features: 9×56 Output weights: $64 \times 96 \times 56$ (Both strain-symmetrized)
Reverse Learning Model: Convolutional Neural Network (CNN) Model				
Strain-symmetrized and strained SLs	$\text{Si}_{2p}\text{Ge}_{2p}$ $(p = 1, 2, \dots, 14)$ $(\text{Si}_{2q-1}\text{Ge}_{2q-1})^2$ $(q = 1, 2, \dots, 7)$ • 5 applied strains: [0.00%, 0.59%, 1.16%, 1.73%, 2.31%] • Total: 126 structures • Atomic environments: $6 \times 4 \times \left(\sum_{i=1}^{14} p_i + \sum_{j=1}^7 (2q_j - 1) \right) = 3696$	• Spectral weights, $A_{E,k}$: $k \times E = 64 \times 64$ per atom • Fermi level alignments: 13 values around -0.5 eV to +0.5 eV of mid-gap level with step of 1/13 eV • Total: $64 \times 64 \times 13 \times 3696$	• Atom type: 1 feature/atom • Effective bond lengths, b_x & b_z : 2 features/atom • Order parameters, $Q_{x,z}^{1,2,3}$: 6 features/atom • Total: 9×3696 features	• HS: $\text{Si}_{24}\text{Ge}_{15}\text{Si}_9\text{Ge}_6\text{Si}_3\text{Ge}_3$ 0.00% strained (on Si substrate) Input ASFs pixels: $64 \times 64 \times 60$ Output features: 9×60 • HS: $\text{Si}_{24}\text{Ge}_{15}\text{Si}_9\text{Ge}_6\text{Si}_3\text{Ge}_3$ strain-symmetrized (see SI Figure 8) Input ASFs pixels: $64 \times 64 \times 60$ Output features: 9×60 • Bulk systems (see SI Table 1)
$(\text{Si}_{2q-1}\text{Ge}_{2q-1})^2 \equiv \text{Si}_{2q-1}\text{Ge}_{2q-1}\text{Si}_{2q-1}\text{Ge}_{2q-1}$ for odd $q = 1, 2, \dots, 7$ SL: Superlattice; HS: Heterostructure;				
Combined Forward-Reverse Learning Framework: NN, RF & CNN				
• Relaxed and 1.73% strained bulk Si CNN Model: Input pixels: 64×64 ; Output features: 9 NN and RF Model: Input features: 9; Output weights: 64×96 • GaAs ARPES spectra CNN Model: Input pixels: 64×64 ; Output features: 9 NN and RF Model: Input features: 9; Output weights: 64×96 • Other bulk Si and Ge systems (see SI Table 1)				

ticle in Table 1. We consider ideal superlattices with sharp interfaces. We consider tetragonal supercells that are periodically extended in the [001] growth direction. We consider strain-symmetrized and strained supercells that represent superlattices grown on substrates [16, 17].

Strain plays a strong role in determining superlattice bands [18–20] and electronic properties [19, 21–24]. We include strained superlattices to train the ML models on band splittings due to strain. We optimize the geometry of all supercells using DFT, see Methods section.

We choose the following two types of descriptors of atom X in a training or a test structure: elemental and structural features. The elemental feature is the atom type: 1 for Si and 0 for Ge. We compute the structural features using crystal graphs, constructed from Voronoi tessellations [15]. The structural features are of two types. (1) The effective bond length, $\bar{l}_i(X)$ of atom X , located at \vec{r}_X , is given by:

$$\bar{l}_i(X) = \frac{\sum_n \omega_{i,n} A_n * \|\vec{r}_n - \vec{r}_X\|_2}{\sum_n \omega_{i,n} A_n}. \quad (1)$$

Here i refers to Cartesian directions, (x, y, z) , \vec{r}_n is the location and A_n is the Voronoi cell face area of the n^{th} neighbor atom. We only consider x and z directions, since structural environments are same along x and y directions. To describe the anisotropy of the bonding environment, we define the weights, $\vec{\omega}$. $\vec{\omega}$ represents the projection of Voronoi cell face area onto the Cartesian planes:

$$\begin{aligned} \vec{\omega}_n &= (\omega_{x,n}, \omega_{y,n}, \omega_{z,n}) \\ &= (\cos^2 \phi_n \sin^2 \theta_n, \sin^2 \phi_n \sin^2 \theta_n, \cos^2 \theta_n). \end{aligned} \quad (2)$$

The angles ϕ_n and θ_n are the polar and azimuthal angles of the interatomic distance vectors between the atom X and the n^{th} neighbor. (2) The order parameters are given by

$$Q_i^{\text{order}}(X) = \sum_{\text{paths}} \prod_{\text{steps}}^{\text{order}} \frac{\omega_{i,n} A_n \delta_{nX}}{\sum_a \omega_{i,a} A_a - \omega_{i,b} A_b}, \quad (3)$$

with $\text{order} = 1, 2, 3$. We consider crystal graphs up to a specified order ($= 3$) neighbor, since higher order graphs do not significantly affect the predictions. $Q_i^{\text{order}}(X)$'s are contributed by paths in the crystal graphs. As indicated by the Kronecker delta in the above equation, δ_{nX} , the graphs have non-zero weights if atom X and neighbor n are same atom types. We provide detailed description of the order parameters in our previous publication, see Supplementary Information [15]. We demonstrate here that these two descriptors are strongly correlated with the character of superlattice bands.

(2) Generation of Spectral Function Training Data

We compute the electronic band structures of the superlattices and the heterostructures in the periodic zone representation of the tetragonal supercells. The different supercell sizes result in different number of bands with varied folding. It is challenging to compare the different band structures and interpret to what extent heterostructure bands differ from their bulk counterparts. Additionally, the supercell bands cannot be directly compared with ARPES spectra. Hence, we unfold the supercell bands into EBS in the extended zone representation of

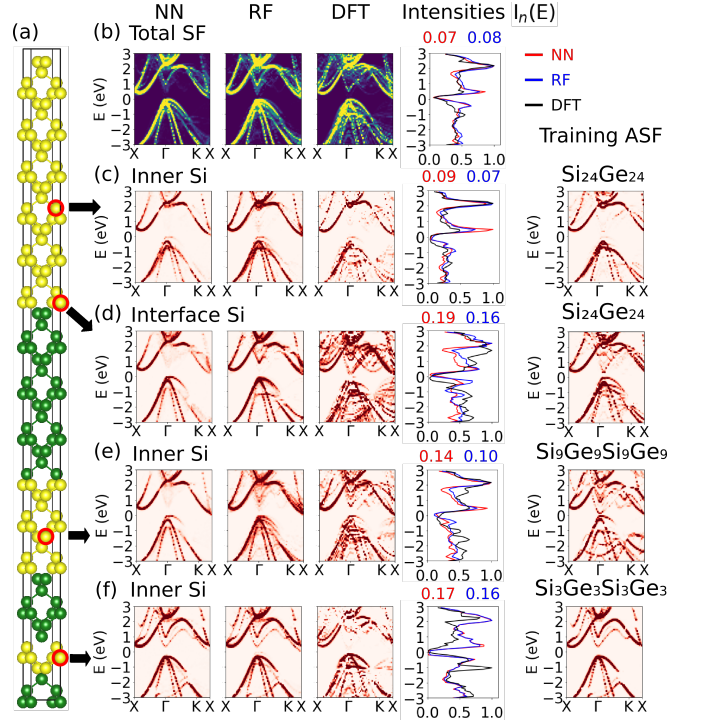


FIG. 2. **Forward learning model predictions:** (a) Representative supercell configuration of a test heterostructure with unevenly thick layers: $\text{Si}_{24}\text{Ge}_{15}\text{Si}_9\text{Ge}_6\text{Si}_3\text{Ge}_3$; (b) Predicted total SF and ASFs of atoms in (c) inner Si_{24} , (d) interface Si_{24} , and inner (e) Si_9 , and (f) Si_3 regions of the heterostructure. NN and RF predictions and DFT results are shown in first, second and third columns of rows (b)-(f), respectively. Fourth column shows comparison between normalized intensities of the SF images, and MAEs for NN (red) and RF (blue) predictions. Last columns show example training data for reference: ASFs of (c) inner and (d) interface Si atoms of $\text{Si}_{24}\text{Ge}_{24}$, and inner Si atoms from (e) $\text{Si}_9\text{Ge}_9\text{Si}_9\text{Ge}_9$, and (f) $\text{Si}_9\text{Ge}_9\text{Si}_9\text{Ge}_9$ superlattices.

chosen reference cells. We choose reference cells that resemble the primitive cell of FCC bulk silicon. Figure 1(b) shows a reference cell corresponding to a Si_4Ge_4 supercell. The reference cell and the supercell are marked with solid red and dashed blue lines, respectively. The reference cell lattice vectors are determined from the supercell lattice vectors through a matrix transformation, see Methods section. The reference cell lattice vectors vary for different supercells, however, all reference cells include two lattice sites. The similar Brillouin zones (BZs) provide a common reference for comparing the unfolded band structures.

The BZ of an example reference cell is shown in Fig. 6(f) in the Methods section. We compute ASF of atoms along the $X - \Gamma - K - X$ path, indicated by the green plane. Figure 1(c) shows representative ASFs, $A^p(k, E)$, for given atom p . Here k values sample the chosen path and $E = -3$ to 3 eV. Each ASF is treated as

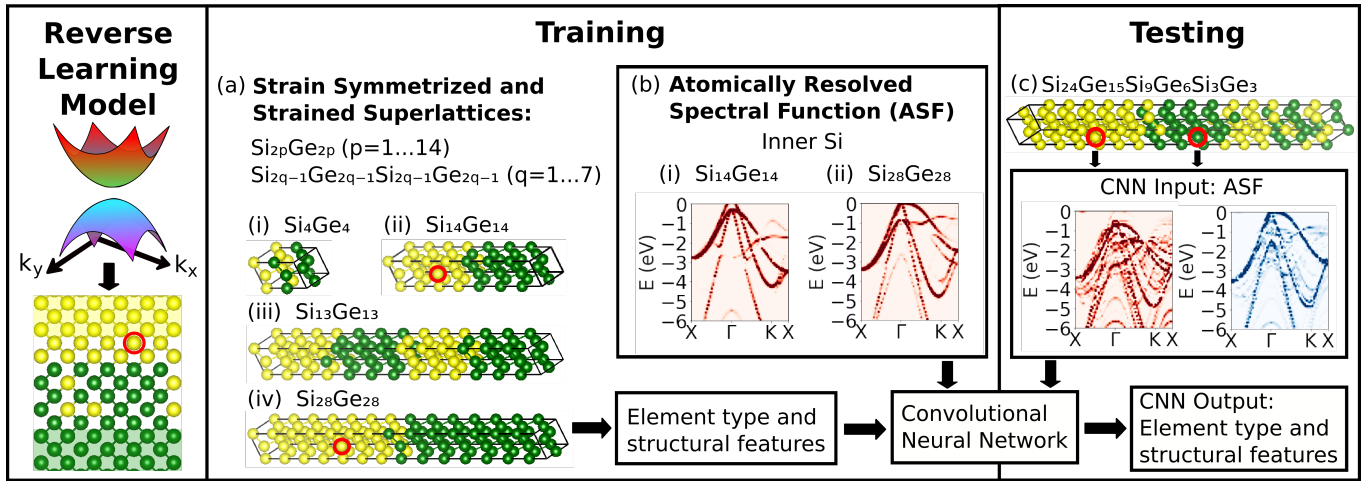


FIG. 3. **Outline of reverse ML model:** (a) Training strain-symmetrized and strained superlattices with varied periods and compositions: (i) Si_4Ge_4 , (ii) $\text{Si}_{14}\text{Ge}_{14}$, (iii) $\text{Si}_{13}\text{Ge}_{13}$ and (iv) $\text{Si}_{28}\text{Ge}_{28}$. Descriptors considered: Element types, bond lengths and order parameters. (b) Property value corresponding to descriptors: Example ASFs of inner Si atoms in (i) $\text{Si}_{14}\text{Ge}_{14}$ and (ii) $\text{Si}_{28}\text{Ge}_{28}$. Trained convolutional neural network (CNN) model predicts atomic environment descriptors for input ASF of atoms in (c) heterostructure, $\text{Si}_{24}\text{Ge}_{15}\text{Si}_9\text{Ge}_6\text{Si}_3\text{Ge}_3$. Predictions are compared with computed descriptors.

an image with 64×64 pixels of resolution. We present a detailed comparative analysis of the SFs of training superlattices in Fig. 1 of Supplementary Information. The analysis reveals that the total SFs of superlattices display a mixture of Si-like and Ge-like character. However, the ASFs of inner atoms in large period superlattices show bulk-like character and do not display a mixed character. The ASFs of short-period superlattices exhibit splitting and mixing of bands and avoided crossing due to strong translational symmetry breaking. Quantifying these band characters is critical both from the fundamental viewpoint and for designing heterostructures for target applications. Our model identifies a relationship between these characters and atomic structural features and rapidly predict bands of complex heterostructures.

(3) Implementation of ML Models

We implement the forward learning approach using neural network (NN) and random forests (RF) models, separately. The models are trained on the relationship between atomic descriptors and respective ASFs of all atoms. We provide the details in Methods section.

(4) Comparison of Predictions with DFT Results

We test the ML model on a heterostructure with multiple Si and Ge layers of randomly chosen thicknesses: $\text{Si}_{24}\text{Ge}_{15}\text{Si}_9\text{Ge}_6\text{Si}_3\text{Ge}_3$ (Fig. 2(a)). Such a configuration is likely to represent fabricated heterostructures with unevenly thick layers. Figure 2(b) shows the total SFs, ob-

tained by summing over all predicted ASFs. The bottom rows show the ASFs from four regions of interest. Instead of comparing SF values and DFT results directly, we obtain the intensity, $I(E)$, at each E by summing over SFs at different k values: $I(E) = \sum_j A(k_j, E)$. The normalized intensities are obtained by dividing $I(E)$ by the maximum intensity: $I_n(E) = I(E)/\text{Max}[I(E)]$. The mean absolute errors (MAEs) are obtained from: $\text{MAE}(I_n, \hat{I}_n) = \sum_E |I_n(E) - \hat{I}_n(E)|/64$. The predicted total SFs display a mixture of Si-like and Ge-like characters and match the DFT results, resulting in small MAEs (NN: 0.07, RF: 0.08). The inner Si ASFs in Si_{24} exhibit a prominent bulk Si character. The predictions are similar to the inner Si ASFs of $\text{Si}_{24}\text{Ge}_{24}$ superlattice, see last column of Fig. 2(c). This result indicates that inner Si atoms in Si_{24} region and in $\text{Si}_{24}\text{Ge}_{24}$ superlattices are in similar bulk-like environments. The high prediction accuracy (NN: 0.09, RF: 0.07) establishes that ML models can learn and predict the local structure-ASF relationships present in varied configurations. However, the accuracy decreases for narrow regions. The NN model predicts prominent bulk Si character for inner ASFs in Si_9 and does not show Ge-like bands near the Γ point, resulting in a higher MAE: 0.14. The RF prediction shows these bands, resulting in a smaller MAE: 0.10. Larger band splittings and changes in Γ character can be noted for narrow Si regions.

The DFT results (third column) exhibit significantly more band splitting, mixing and discontinuities compared to predicted ASFs. When the supercell includes strongly broken translational order, the unfolded contributions from different regions vary, resulting in broken band structures. Additionally, the reference cells may not

represent true irreducible cells for a given heterostructure or superlattice. On the other hand, ML results are interpolated from superlattices of similar periods. The higher translational order results in continuous band structures. The discrepancy is more pronounced for narrow Si layers. Prediction accuracy is also low for interface Si ASFs. The larger error (NN: 0.19, RF: 0.16) can be attributed to training data, that include more bulk information than interfaces. Higher training data results in higher accuracy for inner ASFs than interface ASFs. It can be concluded that the error increases with the increase of number of interfaces in the heterostructure. It is important to remember that the training set does not include such multilayer heterostructures. The error is likely to reduce if the model is trained on such structures.

REVERSE LEARNING MODEL

We show the outline of the reverse learning model in Fig. 3. We choose similar training structures as the forward learning model (see Table 1). We provide the DFT computed ASFs and the descriptors as input. Each ASF is treated as a greyscale image with resolution of 64×64 pixels, with pixel intensities scaled from 0 to 1. We only use ASF data for the energy range between -6 eV to 0 eV as input. We choose this energy range since the available ARPES images scan this energy values. The convolutional neural network (CNN) model predicts the descriptors of atomic environment associated with an input ASF image (Fig. 3(c)). We provide the model details in Methods section. We test the model performance on the heterostructure, $\text{Si}_{24}\text{Ge}_{15}\text{Si}_9\text{Ge}_6\text{Si}_3\text{Ge}_3$, assumed to be grown on a Si substrate. Figure 14 shows the CNN-predicted descriptors for all atoms. The MAE for each descriptor (D) is given by: $MAE(D, \hat{D}) = \sum_i^{p \times n} |D_i - \hat{D}_i| / (p \times n)$, where p is the number of atoms in the test structure and n is the number of different Fermi level alignments ($n = 13$). The model remarkably predicts the variation of atomic descriptors across the heterostructure. The atom types for inner atoms are predicted with higher accuracy than interface atoms. The prediction accuracy decreases for narrow layers. The Si and Ge layers have same in-plane lattice constants, resulting in constant values of b_x 's. Additionally, same b_x and b_z values in the Si regions are imposed by the Si substrate. However, b_z 's in Ge layers (2.73 Å) are higher than those in Si layers (2.58 Å), as expected. The low values of the order parameters near the interfaces indicate that the interface atoms have fewer same species neighbors. As a reference, the order parameters in bulk are equal to 1. The higher order parameter plots clearly show the interface regions for wide layers. However, these plots cannot distinguish narrow layers very well. All panels of Fig. 14 show that the model accuracy is higher for bulk-like inner regions than interfaces or low-symmetry regions. The complex

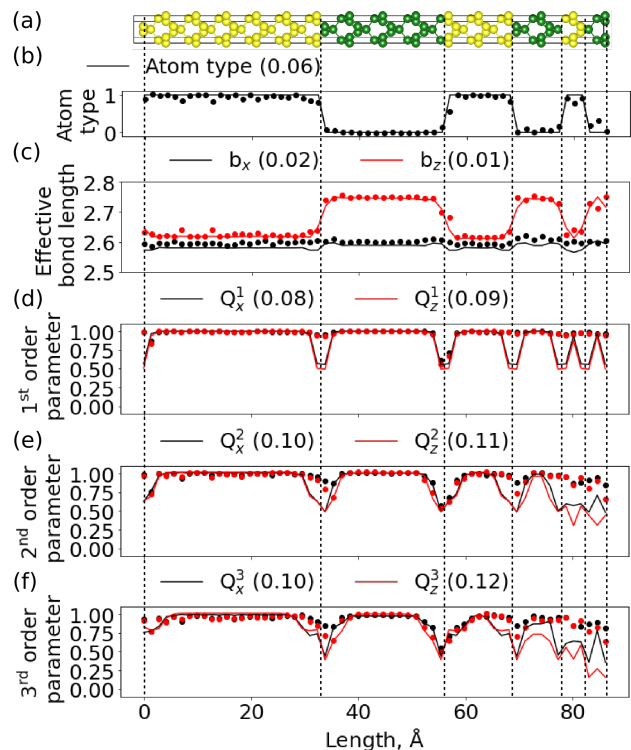


FIG. 4. **Reverse learning model prediction:** (a) Supercell configuration of $\text{Si}_{24}\text{Ge}_{15}\text{Si}_9\text{Ge}_6\text{Si}_3\text{Ge}_3$ with epitaxial strain due to Si substrate; Predicted (b) atom type, (c) effective bond length and (d-f) spatially resolved order parameters, Q_i^{order} where $i = (x, z)$ and $order = 1, 2, 3$, for all atoms. MAEs between predicted (circles) and calculated descriptors (solid lines) are shown next to legends.

character of interface ASFs (Fig. 2(d)) and limited training data result in low accuracy predictions. Additionally, it is important to note that the descriptors are calculated using Voronoi tessellations that is extremely sensitive to atomic environments and introduces uncertainty in the training data and predictions [25, 26].

Proposed Forward-Reverse Learning framework

Figure 5 shows the workflow of the combined forward and reverse learning framework. The CNN module reduces the input SF images to a set of descriptors. We pass the CNN-predicted descriptors to the forward learning models and obtain ASFs. We compare intensities computed from input data and the output of the combined model. We test the framework using DFT computed SF images as well as ARPES spectra of bulk systems. The framework is only trained on superlattices and is not aware about the properties of pristine bulk material. Figure 5 shows the DFT-predicted SF images of (a) bulk and (b) substrate-strained Si (s-Si), respectively. The s-Si model is considered to be grown on $\text{Si}_{0.7}\text{Ge}_{0.3}$ alloy

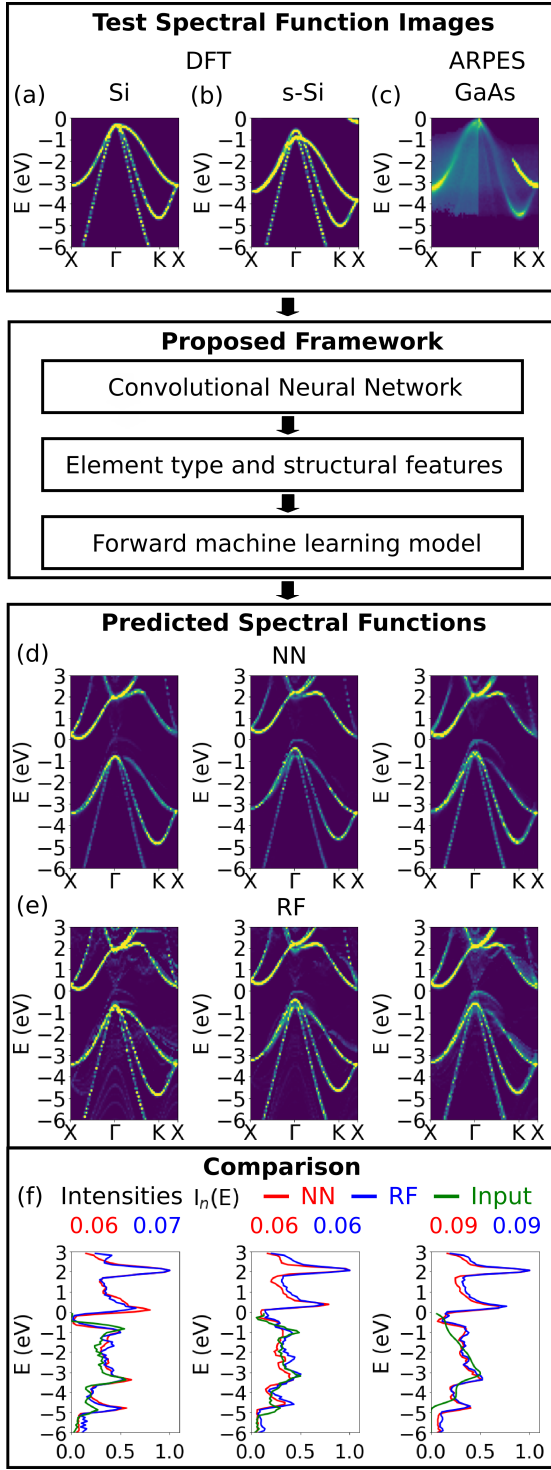


FIG. 5. **Proposed forward-reverse learning framework.** Input images: (a-b) DFT predicted total SFs for (a) relaxed and (b) substrate-strained (s-Si) bulk Si and (c) ARPES spectra of GaAs thin film, adopted from Ref. 27. CNN extracts atomic environment descriptors from input. The descriptors are provided as input to forward learning model. (d) NN and (e) RF-predicted output SFs of corresponding systems. (f) Comparison between predicted normalized intensities and input DFT results (left and middle) and ARPES data (right), respectively. MAEs are shown on top of figure.

substrate, that induces 1.73% in-plane strain. The strain-induced splitting of the valence band maximum can be noted from Fig. 5(b). We list the CNN-predicted descriptors in Table 2. The predicted b_x and b_z values are somewhat higher than the DFT results. However, the trends are well reproduced. For example, b_x is higher than b_z for the system with in-plane strain. The predictions for strained system are closer to DFT results.

Figure 5(c) shows the test ARPES spectra of GaAs thin film, adopted from Fig. 2 of Ref. 27, see Methods section. We choose this test system since the band structure is similar to Ge, especially in the energy range considered. Thus, the test image is similar to images CNN is trained with. We show the CNN-predicted descriptors in Table 2. The model predicts fractional atom types, indicating that atoms are neither Si or Ge. The predicted effective bond lengths are higher than bulk Si. This might correspond to the fact that GaAs lattice constants are higher than Si and closer to Ge. The order parameters are lower than 1, indicating that the atomic environment deviates from pristine bulk structure. The ARPES image represents band dispersion of GaAs buried underneath an amorphous As layer (~ 1 nm). The predicted order parameters seem to describe the atomic environment of experimental samples. However, a systematic analysis is necessary to confirm this observation. The output

TABLE 2. Predicted Descriptors of Bulk Systems

Test Image	type	b_x	b_z	Q_x^1	Q_z^1	Q_x^2	Q_z^2	Q_x^3	Q_z^3
Input: DFT Obtained SFs									
(a) Si	DFT	1.00	2.58	2.58	1.00	1.00	1.00	1.00	1.00
0.00%	CNN	0.99	2.61	2.61	1.00	1.00	1.00	0.99	1.00
(b) s-Si	DFT	1.00	2.63	2.57	1.00	1.00	1.00	1.00	1.00
1.73%	CNN	1.00	2.64	2.59	0.99	1.00	1.00	1.00	0.98
Input: ARPES Spectra									
(c) GaAs	CNN	0.88	2.62	2.62	0.94	0.93	0.85	0.81	0.79

descriptors are provided as input to the forward learning NN and RF models. A larger valence band splitting can be noticed in predicted GaAs SFs. The conduction bands of GaAs are not likely to be accurately represented, although contributions from conduction bands near Γ -point can be noticed. Fig. 5(f) shows the comparison between normalized intensities of the input and the output SF images. We find close agreement for both bulk Si and GaAs models. This test illustrates the remarkable ability of our framework to predict electronic bands of new material from purely structural information.

CONCLUSIONS

We propose a first-principles modeling framework that establishes a direct relationship between atomic struc-

tural features and electronic bands of semiconductor heterostructures. The framework combines a forward and a reverse ML model. The forward model shows that atomic environments, such as neighbor bond lengths, local network of atoms etc, tune heterostructure bands. The different atomic environments determine the Bloch character of heterostructure bands. For example, an inner atom maintains bulk character, however, an interface atom displays complex character such as band splittings, avoided crossings and changes of Γ -characters. The reverse model predicts the atomic environment that is associated with an input band structure image. It is remarkable that the model can predict atom types purely from the valence band character exhibited by an experimental image. We establish that the relationship between structural features and band character is deeply fundamental in nature. We illustrate that this relationship can be leveraged to predict properties of GaAs, even though the framework is trained on Si/Ge systems. The combined model illustrates that atomic environments can be designed to manipulate heterostructure bands and achieve desired electrical, magnetic and optical properties. Our framework offers a physics-informed approach to create layered materials for new phenomena and device possibilities for diverse technologies.

DATA AVAILABILITY

The data supporting the findings of this study are available within the main article and the Supplementary Information document. In addition, we uploaded an example data set in the CUantamLab public GitHub repository [28]. The example data set includes geometry optimized 49 Si/Ge superlattice configurations, both strain-symmetrized and with external strain.

CODE AVAILABILITY

We made the Python scripts available, that can be used for extracting descriptors from the example data set [28].

ACKNOWLEDGEMENTS

We gratefully acknowledge funding from the Defense Advanced Research Projects Agency (Defense Sciences Office) [Agreement No.: HR0011-16-2-0043]. We acknowledge funding from the National Science Foundation Harnessing the Data Revolution NSF-HDR-OAC-1940231. This work utilized the Summit supercomputer, which is supported by the National Science Foundation (awards ACI-1532235 and ACI-1532236), the University of Colorado Boulder, and Colorado State University. The

Summit supercomputer is a joint effort of the University of Colorado Boulder and Colorado State University.

AUTHOR CONTRIBUTIONS

A.K.P contributed to the acquisition and the analysis of data and the creation of new scripts used in the study. S.N. contributed to the conception and the design of the work, the interpretation of data, drafting and revision of the article.

COMPETING INTERESTS

The authors declare no competing interests.

METHODS

Training and Test Structures for All ML Models

Training Structures: We consider ideal superlattices with both even and odd number of monolayers, referred to as $\text{Si}_{2p}\text{Ge}_{2p}$ ($p = 1, 2, \dots, 14$) and $\text{Si}_{2q-1}\text{Ge}_{2q-1}\text{Si}_{2q-1}\text{Ge}_{2q-1}$ ($q = 1, 2, \dots, 7$), respectively. The total number of atoms in model supercells (SCs) of these superlattices are even multiples of four. The SCs of $\text{Si}_{2p}\text{Ge}_{2p}$ configurations include $4p$ atoms and $\text{Si}_{2q-1}\text{Ge}_{2q-1}\text{Si}_{2q-1}\text{Ge}_{2q-1}$ configurations have $4(2q-1)$ atoms. We construct the SCs using a template that includes four atomic positions, as we discuss below. For the superlattices with odd number of monolayers, we double the SC sizes to account for the structure periodicity. We consider both strain symmetrized superlattices and superlattices with applied strains: 0.00%, 0.59%, 1.16%, 1.73%, and 2.31%. The strains are measured relative to bulk Si lattice constant: $((a' - a_{\text{Si}})/a_{\text{Si}}) \times 100$, where $a_{\text{Si}} = 5.47 \text{ \AA}$. The applied in-plane strain values correspond to alloy growth substrates, $\text{Si}_{1-x}\text{Ge}_x$, with varied Ge concentrations: $x = 0, 0.1, 0.2, 0.3, 0.4$.

Test Structures for Forward ML Model: Strain-symmetrized (i) $\text{Si}_{28}\text{Ge}_{28}$ superlattice and (ii) $\text{Si}_{24}\text{Ge}_{15}\text{Si}_9\text{Ge}_6\text{Si}_3\text{Ge}_3$ heterostructure.

Test Structure for Reverse Learning CNN Model: $\text{Si}_{24}\text{Ge}_{15}\text{Si}_9\text{Ge}_6\text{Si}_3\text{Ge}_3$ heterostructure assumed to be grown on silicon substrate.

Supercells: We generate the model SCs for all training and test superlattices and heterostructures, using a four-atom bulk Si tetragonal cell template (Si_4). The template is derived from a bulk Si cubic conventional cell. The template and the cubic cell are shown with blue dashed lines and black solid lines in Fig. 6(a, b), respectively. The volume of the template is half of the volume of the cubic cell. The lattice parameters of the template are given by, $a' = b' = 2.73 \text{ \AA}$ and $c = 5.47 \text{ \AA}$,

following geometry optimization. $c = 5.47\text{\AA}$ is same as lattice constant of bulk Si cubic cell. Our values agree with previous DFT results [29]. Although, it is known that the DFT-predicted lattice constants of bulk Si are $\sim 1\%$ higher than experimental values [30]. The basis vectors of the SC template are given by $a'[\bar{1}10]$, $b'[\bar{1}10]$, and $c[001]$. The template is periodically extended in the $[001]$ growth direction. The template can be used to span a bulk Si system with cubic symmetry, e.g., $[001]$ grown superlattices, by replicating in the $[110]$, $[\bar{1}\bar{1}0]$ and $[001]$ directions. This template allows us to investigate a large variety of superlattices and heterostructures, while keeping the computational expense at a minimum.

The template includes four atomic positions, see Fig. 6. The black, red, blue and green colors, represent atomic positions residing in planes that are $a/4$ apart along $[001]$. Fig. 6(c, d) shows the atomic positions as viewed along the $[001]$ direction. To create the superlattice models we insert Si and Ge atoms in the template atomic positions. For example, we obtain a Si_2Ge_2 superlattice model by inserting Si atoms in the blue and green positions, and Ge atoms in the black and red positions of the template, respectively (Fig. 6(e)). The red '+' symbols show the two Si and the two Ge atoms, while the replicas are unmarked. We obtain strain-symmetrized or strained configurations by performing geometry optimization of the supercell models. To create superlattice models with longer periods, we start with $[001]$ periodically replicated models of SC template. We insert Si and Ge atoms in the atomic positions of the replicated template. That way, the resulting SC includes the desired number of Si and Ge monolayers. A representative eight-atom Si_4Ge_4 superlattice model is shown in Fig. 1(b). Table 3 lists the lattice parameters of all geometry optimized supercells investigated in this article.

Test Structures for Combined Model: Strain-symmetrized and strained bulk Si, modeled with Si_4 SC. The strained model is considered to be grown on $\text{Si}_{0.7}\text{Ge}_{0.3}$ substrate, with 1.73% in-plane strain.

Test ARPES Image for Combined Model: ARPES spectra adopted from Fig. 2 of Ref. 27. We combine the band dispersions along $\Gamma - X$ (Fig. 2(b)) and $\Gamma - K - X$ paths, obtained with s-(Fig. 2(e)) and p-polarization (Fig. 2(d)) into a single image. We interpolate the experimental images from the resolution provided in Ref. [27] to 64×64 pixels in size and for energy range from -6 eV to 0 eV.

DFT Computation Details

We optimize the lattice constants and the atomic positions of training and test SC models with conjugate gradient algorithm [31]. We sample the SC BZ with $11 \times 11 \times 11$ k -point mesh, generated by the Monkhorst-Pack scheme [32]. Although c is generally larger than a' and b' , we use $11 \times 11 \times 11$ k -point mesh to ac-

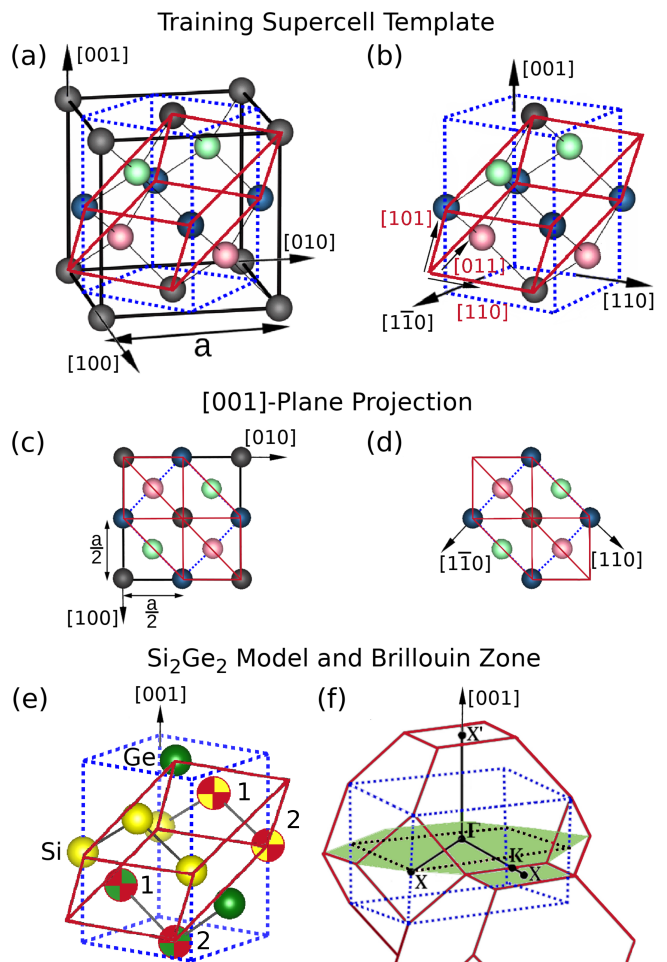


FIG. 6. **Generation of training supercells (SC) and selection of reference cells (RC):** (a, b) Tetragonal SC template (blue dashed lines) generated from a bulk Si conventional cell (black solid lines). a refers to bulk Si lattice constant. SC template includes four atomic positions, with one position per monolayer stacked along $[001]$ direction: black, red, blue and green. Representative two-atom RC chosen for unfolding (solid red lines). (c, d) Atomic positions in Si conventional cell, SC template and RC viewed along the $[001]$ direction. (e) Si_2Ge_2 superlattice SC, with two Si and two Ge atoms marked with red. Other atoms are replicas. Pairs of marked SC atoms ('1' and '2') are mapped to the two corresponding RC atomic positions, respectively. (f) SC (blue) and RC (red) Brillouin zone (BZ). Black dashed line represents projection of SC BZ onto the $[001]$ plane passing through Γ point. Symmetry points and paths in the green plane are used to obtain effective band structures or spectral functions.

commodate for ample sampling along $[001]$. Such sampling is particularly necessary for complex heterostructures with irregularly thick Si or Ge layers. To simulate SC under applied strain, we assign a' and b' to be equal to the substrate lattice constants and relax the cell shape in the cross-plane $[001]$ direction. The DFT calculations reported in this article, are performed using

TABLE 3. Lattice Parameters of Supercells, Å
Basis vectors: $a'[1\bar{1}0]$, $a'[110]$, $c'[001]$

Structures	Strain-Symmetrized		Grown on $\text{Si}_{1-x}\text{Ge}_x$ Substrate Ge concentration, $x =$				
	a'	c'	0.0	0.1	0.2	0.3	0.4
Si_4	2.73	5.47	5.47	5.41	5.35	5.29	5.23
Ge_4	2.89	5.79	6.48	6.40	6.33	6.26	6.19
$(\text{Si}_1\text{Ge}_1)^2$	2.81	5.60	5.93	5.86	5.80	5.73	5.67
Si_2Ge_2	2.81	5.60	5.93	5.86	5.79	5.73	5.66
$(\text{Si}_3\text{Ge}_3)^2$	2.81	16.86	17.79	17.59	17.39	17.19	16.99
Si_4Ge_4	2.81	11.25	11.87	11.73	11.60	11.47	11.34
$(\text{Si}_5\text{Ge}_5)^2$	2.81	28.12	29.66	29.32	28.98	28.66	28.33
Si_6Ge_6	2.81	16.88	17.82	17.61	17.41	17.21	17.02
$(\text{Si}_7\text{Ge}_7)^2$	2.81	39.39	41.55	41.08	40.61	40.15	39.70
Si_8Ge_8	2.81	22.53	23.75	23.48	23.21	22.95	22.69
$(\text{Si}_9\text{Ge}_9)^2$	2.81	50.63	53.44	52.83	52.22	51.63	51.05
$\text{Si}_{10}\text{Ge}_{10}$	2.81	28.15	29.72	29.38	29.04	28.71	28.39
$(\text{Si}_{11}\text{Ge}_{11})^2$	2.81	61.90	65.37	64.62	63.89	63.16	62.45
$\text{Si}_{12}\text{Ge}_{12}$	2.81	33.75	35.65	35.24	34.84	34.44	34.05
$(\text{Si}_{13}\text{Ge}_{13})^2$	2.81	73.10	77.14	76.26	75.39	74.53	73.69
$\text{Si}_{14}\text{Ge}_{14}$	2.81	39.39	41.55	41.07	40.61	40.15	39.69
$\text{Si}_{16}\text{Ge}_{16}$	2.81	45.01	47.51	46.96	46.43	45.90	45.38
$\text{Si}_{18}\text{Ge}_{18}$	2.81	50.65	53.47	52.86	52.26	51.67	51.08
$\text{Si}_{20}\text{Ge}_{20}$	2.81	56.29	59.46	58.78	58.11	57.45	56.80
$\text{Si}_{22}\text{Ge}_{22}$	2.81	61.88	65.27	64.52	63.78	63.06	62.35
$\text{Si}_{24}\text{Ge}_{24}$	2.81	67.55	71.26	70.44	69.64	68.85	68.07
$\text{Si}_{26}\text{Ge}_{26}$	2.81	73.15	77.23	76.34	75.47	74.61	73.77
$\text{Si}_{28}\text{Ge}_{28}$	2.81	78.79	83.20	82.25	81.31	80.39	79.48
HS	2.79	83.91	87.57				
			substrate tuned a'				
			2.73	2.75	2.76	2.78	2.80

$(\text{Si}_q\text{Ge}_q)^2 \equiv \text{Si}_q\text{Ge}_q\text{Si}_q\text{Ge}_q$ for odd $q = 1, 3, 5, 7, 9, 11, 13$
HS: $\text{Si}_{24}\text{Ge}_{15}\text{Si}_9\text{Ge}_6\text{Si}_3\text{Ge}_3$

the OpenMX code which is based on norm-conserving pseudopotentials generated with multiple reference energies [33] and linear combination of optimized pseudoatomic basis functions [34]. We use the Perdew-Burke-Ernzenhof exchange-correlation formulation [35] of the generalized gradient approximation. Self-consistent field (SCF) calculations are performed during the geometry optimization with energy convergence threshold set to 10^{-9} Hartree. The SCs are optimized until the maximum force on an atom became less than 10^{-4} Hartree Bohr $^{-1}$. We use a regular mesh of 200 Ryd in real space for the numerical integrations and solution of Poisson equation [36]. We do not include spin-orbit interaction in our analysis since strain induced band splittings were shown to be larger than the spin-orbit splittings [19]. For the silicon and germanium atoms, 2, 2, and 1 optimized radial functions were allocated for the s-, p- and d-orbitals, respectively, as denoted by s2p2d1. The one-particle wave functions are expressed by the linear combination of pseudo-atomic orbital (PAO) basis functions

centered on atomic site [34, 37]. A cutoff radius of 7.0 Bohr was used for all the basis functions. Following relaxation, we perform non self-consistent field (NSCF) calculations using the linear combinations of atomic orbitals (LCAO) pseudopotential method [34, 37]. We obtain the eigenstates, $|KJ\rangle$ and energy, ϵ_{KJ} , for the range from -10 eV to 10 eV. Here, $|KJ\rangle$ represents a Bloch state with crystal momentum K and band index J , ϵ_{KJ} is the corresponding eigenvalue [38]. We use a $7 \times 7 \times 7$ k-point mesh generated according to the Monkhorst-Pack method [32] to sample the supercell BZ. Such k-point mesh has been used in DFT studies for calculation of electronic structure of two-atom Si lattice [38].

Supercells and Reference Cells

We unfold SC electronic band structures to the BZ of chosen reference cells (RCs) via SFs [6–9, 12, 39]. Figure 6 (a-d) show a representative rhombohedron RC with red solid lines. The embedding cubic conventional cell and the SC template are shown with black solid lines and blue dashed lines, respectively. The volume of the RC is 1/4 the volume of the conventional cell. The RC resembles the two-atom primitive cell of FCC Si lattice. If no symmetry breaker is present in the SC, the RC will be identical to a primitive cell. However, the RC representation is defined purely in a mathematical sense and is valid even in the presence of symmetry-breaking interfaces. The RC basis vectors are determined from SC basis vectors. In general, the SC basis vectors are given by:

$$\vec{B} = \begin{pmatrix} a' & -a' & 0 \\ b' & b' & 0 \\ 0 & 0 & c' \end{pmatrix}, \quad (4)$$

where $a' = b'$ and c' are the SC lattice parameters. The SC and the RC basis vectors are related: $\vec{b} = M\vec{B}$, via a transformation matrix, M , given by

$$M = \begin{pmatrix} -\frac{1}{2} & \frac{1}{2} & \frac{1}{2N} \\ \frac{1}{2} & \frac{1}{2} & \frac{1}{2N} \\ 0 & 1 & 0 \end{pmatrix}, \quad (5)$$

where N represents number of templates stacked along [001] direction in the supercell. N is equal to the total number of atoms in the SC divided by 4. For example, $N = 1$ for Si_2Ge_2 , and $N = 2$ for Si_4Ge_4 and so on. Thus, the RC basis vectors are given by:

$$\vec{b} = \begin{pmatrix} \frac{b'-a'}{2} & \frac{b'+a'}{2} & \frac{c'}{2N} \\ \frac{b'+a'}{2} & \frac{b'-a'}{2} & \frac{c'}{2N} \\ \frac{b'}{2} & \frac{b'}{2} & 0 \end{pmatrix}. \quad (6)$$

As shown in Table 3, a' , b' and c' vary for different superlattices or heterostructures, resulting in different basis

vectors for the corresponding two-atom RCs. Fig. 6(e) shows the RC of a Si_2Ge_2 SC and Fig. 6(f) shows the corresponding BZ. We compute AEBS or ASF of atoms along the path indicated by the green plane, and generate training data. The choice of RCs is not unique. Past tight binding studies extensively discussed the identification of appropriate RCs and the advantage of unfolding SC band structures for predicting electronic properties [7]. We exploit the insights to develop our ML framework. However, these studies emphasize that care must be taken when the symmetry of the SCs is different from the RCs. We discuss the consequences in this article.

Spectral Weights and Spectral Functions

The steps for computing SFs are as follows:

- (i) Geometry optimization of chosen SCs;
 - (ii) Calculating SC eigenstates for a k -point mesh;
 - (iii) Identifying RC and a set of wave vectors $\{k_i\}$ along a chosen path in the respective BZ;
 - (iv) Computing SFs for each atom along the path;
 - (v) Repeating steps (i)–(iv) for a different SC;
- Below we discuss the approach used for step (iv).

In the LCAO method, a Bloch state $|KJ\rangle$ is expanded in the form of a linear combination of atomic basis functions, $|RN\rangle$, as

$$|KJ\rangle = \sum_N C_N^{KJ} |KN\rangle, \quad (7)$$

while,

$$|KN\rangle = \frac{1}{\sqrt{L}} \sum_R e^{i\mathbf{K}\cdot\mathbf{R}} |RN\rangle. \quad (8)$$

Here, C_N^{KJ} are the LCAO coefficients. The atomic basis functions, $|RN\rangle$, are placed in every unit cell and specified with a translational lattice vector R . N represents a symbolic orbital index, that consists of the atomic position relative to R , a multiplicity index for radial functions, an angular momentum quantum number, and a magnetic quantum number. L is the number of unit cells included in the Born-von Karman boundary condition. We unfold the SC band structures to RC BZs via SFs, $\hat{A}(E)$, following the method proposed in Ref. [9]. It can be shown that the SF expressions in the SC and the RC representations are related via

$$\begin{aligned} & A_{kj,kj}(E) \\ &= \sum_{mnK} S_{mn}^{-1}(k) \langle kn|KJ\rangle A_{KJ,KJ}(E) \langle KJ|km\rangle. \end{aligned} \quad (9)$$

Here, $|kj\rangle$ is a Bloch state and m and n represent symbolic orbital indices in the RC representations. $S_{mn}(k)$ are the overlap matrix elements. The spectral function,

$A_{kj,kj}(E)$, can be represented as a linear combination of unfolded spectral weights, W_{KJ}^k [9]:

$$A_{kj,kj}(E) = \sum_K W_{KJ}^k A_{KJ,KJ}(E) \quad (10)$$

with

$$\begin{aligned} W_{KJ}^k &= \frac{L}{l} \sum_G \delta_{k-G,K} \\ &\times \sum_{MNr} e^{i\mathbf{k}\cdot(\mathbf{r}-\mathbf{r}'(M))} C_M^{KJ} C_N^{KJ*} S_{0N,rm(M)}. \end{aligned} \quad (11)$$

Here, L and l are the number of unit cells in SC and RC, respectively. $r'(M)$ and $m(M)$ refer to lattice vectors and orbital indices of the RC atomic basis, respectively, that correspond to the SC symbolic orbital index M . The delta function, $\delta_{k-G,K}$ signifies that W at k is contributed only by the folded Bloch state with $k - G = K$, where G is a reciprocal lattice vector. The spectral weights are determined by the phase factor $e^{i\mathbf{k}\cdot(\mathbf{r}-\mathbf{r}'(M))}$, LCAO coefficients, $C_{M \text{ or } N}^{KJ}$, and overlap matrix elements, $S_{0N,rm(M)}$. In the LCAO method, we allocate same basis functions for each atomic species in the SCs with varied periods and compositions. However, same AOs contribute differently to the electronic bands of different SCs due to structural features. The influence of atomic structures is recorded in the LCAO coefficients and the overlap integrals between basis functions. It is important to note that the spectral weights are calculated in the SC representation without relying on any RC details. Thus, unfolding is performed purely in a mathematical sense and is valid as long as a RC can be defined.

Additionally, we compute the atomically resolved SFs that allow us to analyze how spectral weights vary based on the atomic environment. To obtain ASFs, we express the orbitally resolved SFs as:

$$A_{kj,kj}^M(E) = \sum_K A_{KJ,KJ}(E) W_{KJM}^k, \quad (12)$$

where, the orbitally resolved spectral weights, W_{KJM}^k , are given by

$$\begin{aligned} W_{KJM}^k &= \frac{L}{l} \sum_G \delta_{k-G,K} C_M^{KJ} \\ &\times \sum_{Nr} e^{i\mathbf{k}\cdot(\mathbf{r}-\mathbf{r}'(M))} C_N^{KJ*} S_{0N,rm(M)}, \end{aligned} \quad (13)$$

and are obtained by rearranging Eq. 11. Equation 10 can then be written as:

$$A_{kj,kj}(E) = \sum_M A_{kj,kj}^M(E) = \sum_K A_{KJ,KJ}(E) \sum_M W_{KJM}^k. \quad (14)$$

The values of index M depend on the SC size and the number of basis functions for each atom. As an example, for a supercell with n atoms and m basis function

per atom, M ranges from 1 to $n \times m$. By decomposing the spectral weights and the SFs, it is possible to analyze the contribution from different localized basis functions to bands. We obtain the atomically resolved SFs from the orbitally resolved SFs. Considering that there are m basis functions assigned to the p^{th} atom in the supercell: $\{p_1, \dots, p_m\} \subset M$, we add p_m orbitally resolved spectral weights, $W_{KJp_m}^k$, to obtain the ASFs for each atom. Thus, total SF can then be written as:

$$A_{kj,kj}(E) = \sum_K A_{KJ,KJ}(E) \sum_p \sum_{m \subset M} W_{KJp_m}^k, \quad (15)$$

or, in terms of the atomically resolved SFs, $A_{kj,kj}^p(E)$,

$$A_{kj,kj}(E) = \sum_p A_{kj,kj}^p(E) = \sum_p \sum_{m \subset M} A_{kj,kj}^{p_m}(E). \quad (16)$$

Here, $A_{KJ,KJ}(E)$ is a delta function, $\delta(E - \epsilon_{KJ})$.

We obtain the SC eigenstates (ϵ_{KJ}) for the energy range from -10 eV to 10 eV from the NSCF calculations. We compute spectral weights by unfolding the SC eigenstates, $|KJ\rangle$, on RC Bloch states $|k_i j\rangle$. We choose a set of 100 wave vectors $\{k_i\}$ along the $X - \Gamma - K - X$ path of the RC Brillouin zone (as depicted in Fig. 6(f)). We do not explicitly keep track of the band indices and drop the subscript j . The spectral weights are then convoluted with the above delta function to obtain $A_{k,k}^p(E)$ or $A^p(k, E)$. We model the delta function $\delta(E - \epsilon_{KJ})$ representing $A_{KJ,KJ}(E)$ with an exponential function with width 0.02 eV. For the forward ML model, we use a 450 point sampling for the delta function between $-6 \text{ eV} \leq E \leq 3 \text{ eV}$. We then interpolate over 300×450 values of $A^p(k, E)$ and obtain 64×96 ASF values. The ASFs, $A^p(k, E)$, are defined over $\{k\} \rightarrow X - \Gamma - K - X$ and $-6 \text{ eV} \leq E \leq 3 \text{ eV}$. The total SFs, $A(k, E)$, are obtained by summing over $A^p(k, E)$ for all atoms in the superlattice or heterostructure. $A(k, E)$'s are also defined over the same k and E range, with a 64×96 sampling. In the last part of this study, while comparing with the ARPES spectra, we use a 300 point sampling for $-6 \text{ eV} \leq E \leq 0 \text{ eV}$, using 0.02 eV wide delta-function. We choose 300 $\{k_i\}$ vectors along $X - \Gamma - K - X$ to keep a square grid for (k, E) .

ML Model Implementations

Forward Learning Approach: We implement the forward learning approach using NN and RF model, separately. **NN model:** Table 4 shows the layers, the number of nodes in each layer and the activation functions of the NN model. The model has four fully-connected (dense) layers represented by the four rows. The input layer with 32 nodes is followed by two hidden layers with 64 and 128 nodes, respectively. Rectified Linear Unit (ReLU) activation functions are implemented for the input and the hidden layers. The number of input parameters is equal to

number of features considered, nine in our case as shown in Table 1. The output layer has 6144 nodes and linear activation function. The number of nodes in the output layer corresponds to the 64×96 interpolated $A^p(k, E)$ values for the respective superlattice or heterostructure. The same NN model architecture can be employed even when the size of input or output data is changed.

TABLE 4. NN model for forward learning

Layer	Nodes	Parameters
Dense	(32)	input dimension = 9 features $f_a = \text{ReLU}$
Dense	(64)	$f_a = \text{ReLU}$
Dense	(128)	$f_a = \text{ReLU}$
Dense	(6144)	$f_a = \text{Linear}$
$64 \times 96 A^p(k, E)$		

We allocate 25% of training data for model validation. We sample random batches of size 32 sequentially from the training set (e.g., 32/3360) at each epoch during training. The last batch will be of size less than 32 if the remainder is not zero. We update the weights iteratively for 5000 epochs till MAE between predicted and validation ASF:

$$MAE(A^p, \hat{A}^p) = \frac{\sum_{k,E} |A^p(k, E) - \hat{A}^p(k, E)|}{64 \times 96}, \quad (17)$$

reaches a minimum. We employ the ADAM stochastic optimization method for gradient descent [40] with learning rate of 0.0005 to minimize the loss function, MAE in this case. We changed the number of epochs for the NN model from 4000 to 5000 and the error only changed from 0.02187 to 0.02183 (see SI Fig. 6). We are reporting the results obtained with epoch 4840 and MAE 0.02183. The high-level NNs are implemented using the Python Keras library [41]. The optimized weights are used to predict ASF values for test structures.

RF model: The RF model assembles results of several decision trees. Each tree is built from a random selection of training data that include both structural features and ASF of training superlattices. We use feature based decision rules to partition the training data into subsets. As an example, decision rule could be based on order parameter values, e.g., $Q^{x,1}$ in the range 0.5 – 0.6, representing different atomic environments (see Fig. 14). Training data with $Q^{x,1}$ in the range 0.5 – 0.6 could form a subset. The branches of the trees are constituted from the decision rules that identify features that minimize the intrasubset variation of ASF. ASF that maximizes fitting over the subset data are assigned as leaves of the tree. The tree generation process is then repeated for other random subsets of training data. We average over the predicted $A^p(k, E)$ from all the trees to obtain the final predictions. We implement the RF module available in

the scikit-learn Python package [42]. We use 100 regression trees per ensemble and default values for all other parameters recommended for the package. We use input and output same as the NN model, as listed in Table 4. Reverse Learning Approach: We implement the reverse learning approach using CNN model. CNN model is extensively used for feature extraction in digital images and is able to assemble complex patterns from small training data [43]. We employ CNN to identify patterns in the training images of ASFs. The patterns of ASF images represent effects of translational symmetry breaking on the electronic bands of heterostructures. We use the CNN model to learn the relationships between these patterns and the descriptors. The details of the model are shown in Table 5. The model includes one coordi-

TABLE 5. Reverse CNN block

Layer	Shape	Parameters
CoordinateChannel2D	(64, 64, 4)	—
Conv2D	(32, 32, 64)	k=3, s=2 f_a =Softmax
BatchNormalization	—	—
MaxPooling2D	(16, 16, 64)	k=2, s=2
Conv2D	(16, 16, 64)	k=3, s=1 f_a =Softmax
BatchNormalization	—	—
MaxPooling2D	(8, 8, 64)	k=2, s=2
Conv2D	(8, 8, 64)	k=3, s=1 f_a =Softmax
BatchNormalization	—	—
MaxPooling2D	(4, 4, 64)	k=2, s=2
Flatten	(1024)	—
Dense	(128)	f_a =Softplus
Dense	(128)	f_a =Softmax
Dense	($n = 9$ features)	f_a =Linear

k: kernel size, s: stride size, f_a : activation function

nate channel layer (CoordinateChannel2D) [44] and three convolution layers (Conv2D), with 4, 64, 64, and 64 filters each. Each convolution layers is followed by batch normalization and a max pooling layer (MaxPooling2D). The dimension of the tensor at the input layer is (64, 64, 4), where the first two are the pixel dimensions of the image, and the third is the number of filters. The 64×64 pixels of $A^p(k, E)$ images are provided as input. Two fully connected layers (Dense) with 128 nodes with Softplus and Softmax activation function respectively are followed by an output layer (Dense) with linear activation function. The set of descriptors outlined above are passed through the output layer. We consider 3 different sets of descriptors in the model, namely, continuous unbounded (effective bond length), continuous bounded (order parameters), and discrete (atom type). We find that the linear activation function in the output layer is suitable for all the above predictors.

We consider 13 different Fermi level alignments. We

shift the mid-gap DFT zero energy level of the SFs of each configurations by a value dE in the range from -0.5 eV to +0.5 eV with a step of 1/13 eV. The alignments serve a role of electron doping level in ARPES experiments. This training helps the model to predict the descriptors of ARPES images with different Fermi level alignments. We allocate 30% of training data for model validation. We sample random batches of size 64 sequentially from the training set at each epoch during training. We employ the ADAM stochastic optimization method for gradient descent [40] with learning rate of 0.0005 to minimize the loss function. We update the weights iteratively for 2000 epochs till the MAE between predicted and validation descriptors reaches a minimum.

Combined Forward-Reverse Learning Model: Finally, we merge the forward and reverse trained ML models shown in Tables 5 and 4, respectively, into one combined model.

* sanghamitra.neogi@colorado.edu

- [1] Alferov, Z. I. Nobel lecture: The double heterostructure concept and its applications in physics, electronics, and technology. *Rev. Mod. Phys.* **73**, 767 (2001).
- [2] Paul, D. J. Si/SiGe heterostructures: from material and physics to devices and circuits. *Semicond. Sci. Technol.* **19**, R75 (2004).
- [3] David, T. *et al.* New strategies for producing defect free sige strained nanolayers. *Scientific reports* **8**, 1–10 (2018).
- [4] Chen, P. *et al.* Role of surface-segregation-driven intermixing on the thermal transport through planar si/ge superlattices. *Physical review letters* **111**, 115901 (2013).
- [5] Ku, W., Berlijn, T., Lee, C.-C. *et al.* Unfolding first-principles band structures. *Physical review letters* **104**, 216401 (2010).
- [6] Popescu, V. & Zunger, A. Extracting E versus k effective band structure from supercell calculations on alloys and impurities. *Physical Review B* **85**, 085201 (2012).
- [7] Boykin, T. B., Kharche, N. & Klimeck, G. Brillouin-zone unfolding of perfect supercells having nonequivalent primitive cells illustrated with a si/ge tight-binding parameterization. *Physical Review B* **76**, 035310 (2007).
- [8] Boykin, T. B., Kharche, N. & Klimeck, G. Non-primitive rectangular cells for tight-binding electronic structure calculations. *Physica E: Low-dimensional Systems and Nanostructures* **41**, 490–494 (2009).
- [9] Lee, C.-C., Yamada-Takamura, Y. & Ozaki, T. Unfolding method for first-principles LCAO electronic structure calculations. *Journal of Physics: Condensed Matter* **25**, 345501 (2013).
- [10] Chen, M. & Weinert, M. Layer k-projection and unfolding electronic bands at interfaces. *Physical Review B* **98**, 245421 (2018).
- [11] Popescu, V. & Zunger, A. Effective band structure of random alloys. *Physical review letters* **104**, 236403 (2010).
- [12] Boykin, T. B., Kharche, N., Klimeck, G. & Korkusinski, M. Approximate bandstructures of semiconductor alloys from tight-binding supercell calculations. *J. Phys.: Condens. Matter* **19**, 036203 (2007).
- [13] Vasudevan, R., Pilia, G. & Balachandran, P. V. Ma-

- chine learning for materials design and discovery (2021).
- [14] Banjade, H. R. *et al.* Structure motif-centric learning framework for inorganic crystalline systems. *Science advances* **7**, eabf1754 (2021).
- [15] Pimachev, A. K. & Neogi, S. First-principles prediction of electronic transport in fabricated semiconductor heterostructures via physics-aware machine learning. *npj Computational Materials* **7**, 93 (2021).
- [16] d’Avezac, M., Luo, J.-W., Chanier, T. & Zunger, A. Genetic-algorithm discovery of a direct-gap and optically allowed superstructure from indirect-gap si and ge semiconductors. *Physical review letters* **108**, 027401 (2012).
- [17] Zhang, L., Luo, J.-W., Saraiva, A., Koiller, B. & Zunger, A. Genetic design of enhanced valley splitting towards a spin qubit in silicon. *Nature communications* **4**, 1–7 (2013).
- [18] Satpathy, S., Martin, R. M. & Van de Walle, C. G. Electronic properties of the (100)(si)/(ge) strained-layer superlattices. *Physical Review B* **38**, 13237 (1988).
- [19] Hybertsen, M. S. & Schlüter, M. Theory of optical transitions in si/ge (001) strained-layer superlattices. *Physical Review B* **36**, 9683 (1987).
- [20] Tserbak, C., Polatoglou, H. & Theodorou, G. Unified approach to the electronic structure of strained si/ge superlattices. *Physical Review B* **47**, 7104 (1993).
- [21] Proshchenko, V. S., Settipalli, M. & Neogi, S. Optimization of seebeck coefficients of strain-symmetrized semiconductor heterostructures. *Applied Physics Letters* **115**, 211602 (2019).
- [22] Proshchenko, V. S., Settipalli, M., Pimachev, A. K. & Neogi, S. Role of substrate strain to tune energy bands–seebeck relationship in semiconductor heterostructures. *Journal of Applied Physics* **129**, 025301 (2021).
- [23] Settipalli, M. & Neogi, S. Theoretical prediction of enhanced thermopower in n-doped si/ge superlattices using effective mass approximation. *Journal of Electronic Materials* **49**, 4431–4442 (2020).
- [24] Settipalli, M., Proshchenko, V. S. & Neogi, S. The effect of electron–phonon and electron–impurity scattering on the electronic transport properties of silicon/germanium superlattices. *Journal of Materials Chemistry C* **10**, 7525–7542 (2022).
- [25] Leonardi, A., Leoni, M., Li, M. & Scardi, P. Strain in atomistic models of nanocrystalline clusters. *Journal of Nanoscience and Nanotechnology* **12**, 8546–8553 (2012).
- [26] Garg, P. & Rupert, T. J. Grain incompatibility determines the local structure of amorphous grain boundary complexions. *Acta Materialia* **244**, 118599 (2023).
- [27] Kobayashi, M. *et al.* Digging up bulk band dispersion buried under a passivation layer. *Applied Physics Letters* **101**, 242103 (2012).
- [28] Cuantam lab - github page. <https://github.com/CUANTAM>.
- [29] Wright, A. Density-functional-theory calculations for the silicon vacancy. *Physical Review B* **74**, 165116 (2006).
- [30] Semiconductor, V. *General Properties of Si, Ge, SiGe, SiO₂ and Si₃N₄* (2002).
- [31] Press, W. H., Teukolsky, S. A., Vetterling, W. T. & Flannery, B. P. *Numerical Recipes in Fortran 90: Numerical recipes in Fortran 77V. 2. Numerical recipes in Fortran 90* (Cambridge University Press, 1996).
- [32] Monkhorst, H. J. & Pack, J. D. Special points for brillouin-zone integrations. *Physical review B* **13**, 5188 (1976).
- [33] Morrison, I., Bylander, D. & Kleinman, L. Nonlocal hermitian norm-conserving vanderbilt pseudopotential. *Physical Review B* **47**, 6728 (1993).
- [34] Ozaki, T. Variationally optimized atomic orbitals for large-scale electronic structures. *Physical Review B* **67**, 155108 (2003).
- [35] Perdew, J. P., Burke, K. & Ernzerhof, M. Generalized gradient approximation made simple. *Physical review letters* **77**, 3865 (1996).
- [36] Soler, J. M. *et al.* The siesta method for ab initio order-n materials simulation. *Journal of Physics: Condensed Matter* **14**, 2745 (2002).
- [37] Ozaki, T. & Kino, H. Numerical atomic basis orbitals from h to kr. *Physical Review B* **69**, 195113 (2004).
- [38] Bystrom, K., Broberg, D., Dwaraknath, S., Persson, K. A. & Asta, M. Pawpyseed: Perturbation-extrapolation band shifting corrections for point defect calculations. *arXiv preprint arXiv:1904.11572* (2019).
- [39] Lee, Y.-T., Lee, C.-C., Fukuda, M. & Ozaki, T. Unfolding optical transition weights of impurity materials for first-principles LCAO electronic structure calculations. *Physical Review B* **102**, 075143 (2020).
- [40] Kingma, D. P. & Ba, J. Adam: A method for stochastic optimization. *arXiv preprint arXiv:1412.6980* (2014).
- [41] Chollet, F. *et al.* Keras (2015). URL <https://github.com/fchollet/keras>.
- [42] Pedregosa, F. *et al.* Scikit-learn: Machine learning in python. *Journal of machine learning research* **12**, 2825–2830 (2011).
- [43] Sharma, A., Vans, E., Shigemizu, D., Boroevich, K. A. & Tsunoda, T. Deepinsight: A methodology to transform a non-image data to an image for convolution neural network architecture. *Scientific reports* **9**, 1–7 (2019).
- [44] Liu, R. *et al.* An intriguing failing of convolutional neural networks and the coordconv solution. *Advances in neural information processing systems* **31** (2018).
- [45] Eales, T. D. *et al.* Ge_{1-x}Sn_x alloys: consequences of band mixing effects for the evolution of the band gap γ -character with sn concentration. *Scientific reports* **9**, 1–10 (2019).
- [46] Froyen, S., Wood, D. & Zunger, A. Structural and electronic properties of epitaxial thin-layer si n ge n superlattices. *Physical Review B* **37**, 6893 (1988).
- [47] Niquet, Y.-M., Rideau, D., Tavernier, C., Jaouen, H. & Blase, X. Onsite matrix elements of the tight-binding hamiltonian of a strained crystal: Application to silicon, germanium, and their alloys. *Physical Review B* **79**, 245201 (2009).
- [48] Perdew, J. P. Density functional theory and the band gap problem. *International Journal of Quantum Chemistry* **30**, 451–451 (1986).
- [49] Perdew, J. P. *et al.* Understanding band gaps of solids in generalized kohn–sham theory. *Proceedings of the National Academy of Sciences* **114**, 2801–2806 (2017).
- [50] Morales-García, Á., Valero, R. & Illas, F. An empirical, yet practical way to predict the band gap in solids by using density functional band structure calculations. *The Journal of Physical Chemistry C* **121**, 18862–18866 (2017).
- [51] Yu, D., Zhang, Y. & Liu, F. First-principles study of electronic properties of biaxially strained silicon: Effects on charge carrier mobility. *Physical Review B* **78**, 245204 (2008).

- [52] Hinsche, N. F., Mertig, I. & Zahn, P. Effect of strain on the thermoelectric properties of silicon: an ab initio study. *Journal of Physics: Condensed Matter* **23**, 295502 (2011).
- [53] Proshchenko, V. S., Dholabhai, P. P., Sterling, T. C. & Neogi, S. Heat and charge transport in bulk semiconductors with interstitial defects. *Physical Review B* **99**, 014207 (2019).
- [54] Hinsche, N., Mertig, I. & Zahn, P. Thermoelectric transport in strained si and si/ge heterostructures. *Journal of Physics: Condensed Matter* **24**, 275501 (2012).
- [55] Heyd, J., Scuseria, G. E. & Ernzerhof, M. Hybrid functionals based on a screened coulomb potential. *Journal of chemical physics* **118**, 8207–8215 (2003).
- [56] Hummer, K., Harl, J. & Kresse, G. Heyd-scuseria-ernzerhof hybrid functional for calculating the lattice dynamics of semiconductors. *Physical Review B* **80**, 115205 (2009).
- [57] Stephenson, C. *et al.* Band structure of germanium carbides for direct bandgap silicon photonics. *Journal of Applied Physics* **120**, 053102 (2016).

SUPPLEMENTARY INFORMATION

ATOMICALLY RESOLVED SPECTRAL FUNCTIONS OF SUPERLATTICES

Figure 7 shows spectral functions (SFs) of (a) bulk Si and (b) bulk Ge, and the progression of SFs of representative Si/Ge superlattices with decreasing period: (c) $\text{Si}_{26}\text{Ge}_{26}$, (d) $\text{Si}_{20}\text{Ge}_{20}$, (e) $\text{Si}_{12}\text{Ge}_{12}$, (f) Si_6Ge_6 , and (g) Si_4Ge_4 , respectively. The first column (i) represents the total SF and the columns (ii) and (iii) represent ASFs for atoms in the inner Si regions (red) and the inner Ge atoms (blue) of the superlattices, respectively. We show the inner Si and the Ge ASFs separately, to highlight how ASF differs for different atoms within the same superlattice. We compute ASFs for each atom in the superlattices and include in the training data. The results displayed in columns (ii) and (iii) of rows (c)-(h) represent the training data used in our forward ML models. The SFs are shown along $X - \Gamma - K - X$ path in the BZ of the reference cells, respectively. Representative BZ and the symmetry path are illustrated in Fig. 6 in the Methods section. We leverage the ML framework to average over the ASFs for each atomic environment in the training superlattices. We hypothesize that these data encompass the information needed to relate atomic environments in superlattices and resulting evolution of the band characters.

It is expected that the unfolded superlattice bands will display an average character of the folded bulk Si and Ge bands [18]. The total SF of $\text{Si}_{26}\text{Ge}_{26}$ superlattice in panel (c-i), displays a mixture bulk Si and Ge band characters. Similar observation can be made for the total SF of $\text{Si}_{20}\text{Ge}_{20}$ as well. However, it is interesting to note that the inner Si ASFs (c-ii, d-ii) of these two large period

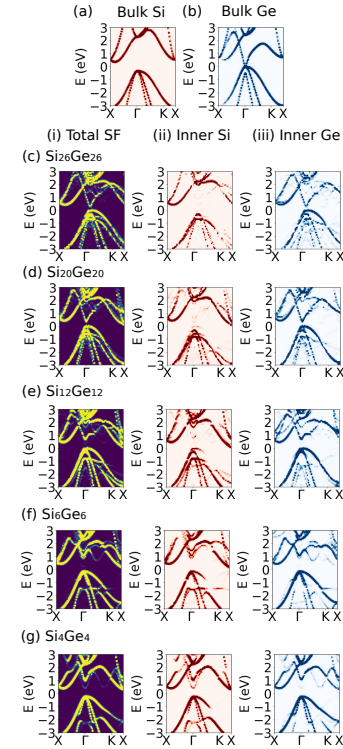


FIG. 7. **Example spectral functions (SFs) of Si/Ge systems investigated in this work:** SFs of bulk (a) Si and (b) Ge. (i) Total SFs and ASFs of (ii) inner Si and (iii) inner Ge atoms in (c) $\text{Si}_{26}\text{Ge}_{26}$, (d) $\text{Si}_{20}\text{Ge}_{20}$, (e) $\text{Si}_{12}\text{Ge}_{12}$, (f) Si_6Ge_6 and (g) Si_4Ge_4 superlattices.

superlattices ($\text{Si}_{26}\text{Ge}_{26}$ and $\text{Si}_{20}\text{Ge}_{20}$) retain prominent bulk Si character. Similarly, the inner Ge ASFs (c-iii, d-iii) retain bulk Ge character. In general, these results show that the inner atom ASFs in large period superlattices primarily maintain the bulk band character and do not display a mixed character. However, we can identify the distinguishing characters of the superlattice bands (e.g., spitting or mixing of bands), upon a closer comparison between inner ASFs and bulk SFs. We discuss the comparison between bulk Si SF and inner Si ASFs. However, similar analysis can be done for Ge as well.

Splitting of bands: The inner ASFs of both $\text{Si}_{26}\text{Ge}_{26}$ and $\text{Si}_{20}\text{Ge}_{20}$ exhibit splitting of the bulk-like bands, especially near the Γ point. The degeneracy of the valence-band maxima at the Γ point is lifted and the bands are split. In an earlier publication, we illustrated that lattice strain in superlattices induces splitting of the valence bands, using Si_4Ge_4 as an example [22]. Strain originates due to the lattice mismatch between Si and Ge layers as well as due to growth substrates. The threefold degenerate states that form the bulk Si valence band maximum split into two approximately degenerate p_x, p_y states and one nondegenerate p_z state [18–20]. The p_x, p_y states form the valence-band edge in Si_4Ge_4 and the p_z state

splits off [22]. The band splittings exhibited by the ASF of $\text{Si}_{26}\text{Ge}_{26}$ and other superlattices are induced similarly by lattice strain. However, the order of the split states and the magnitude of the splitting depends on the specific strain environments. Additionally, Si and Ge layers experience different strains in a given superlattice. This causes leading to different strain induced band splittings for Si and Ge valence bands, as can be noted from (c-ii) and (c-iii). Valence band splittings are also exhibited by $\text{Si}_{12}\text{Ge}_{12}$ and other short-period superlattices. The conduction bands of short-period superlattices show splittings near the Γ point. Figure 7 illustrates the direct relationship between lattice strain environments and character of superlattice bands such as band splitting.

Mixing of bands and avoided crossing: The plots also illustrate that the valence bands of the superlattices exhibit a mixed Si-Ge character. This can be particularly noted from the ASFs of $\text{Si}_{12}\text{Ge}_{12}$ and Si_6Ge_6 , shown in rows (e) and (f), respectively. The inner Si ASFs of these superlattices do not display band dispersions around -1 eV energy level, along the path $\Gamma - K$. However, the total SFs show continuous dispersions in this region. Upon considering column (iii), it can be concluded that the Ge bands mostly contribute to the total SFs in this region. The effect of strain on this mixed bands is complex. Varied strain environments in Si and Ge layers modulate the Si and Ge contributions differently. As can be noted from (e-ii) and (e-iii), the gaps between valence band edge and split-off states are different for Si and Ge ASFs. These split-off bands then affect each other. The split-off Si bands of $\text{Si}_{12}\text{Ge}_{12}$ and Si_6Ge_6 superlattices exhibit signature of avoided crossing due to the split-off Ge bands. The splittings are larger for smaller period superlattices and the indication of avoided crossing is more pronounced. Signatures of avoided crossing can be noted from the conduction bands of Si_6Ge_6 and Si_4Ge_4 superlattices, midway along $X - \Gamma$ and $\Gamma - K - X$ paths.

Folding of bands: The reference cells are mathematical constructions and may not represent true irreducible cells for a given heterostructure or superlattice. When the chosen reference cells do not capture full translational symmetry of the supercells, some residual folded bands are likely to appear. For example, signature of folded bands can be observed along with band discontinuities in ASFs of Si_4Ge_4 superlattice, as shown in Fig. 7(g). This characteristics is particularly visible for short-period superlattices, with strong translational symmetry breaking. The comparison of the band dispersions along $X - \Gamma$ and $\Gamma - K - X$, reveals that ASFs experience more changes along the later symmetry direction. This can be understood by considering the BZ of the reference cell presented in Fig. 6 in the Methods section. The $\Gamma - K - X$ path spans two BZs. Therefore, varied contributions are expected to result in a range of features.

Change of Γ -character: The Γ -character of the bands of the large period superlattices (rows (c) and (d)) is

primarily determined by Ge contributions. As the layer thickness decreases to 12 monolayers or below, the Γ -character is influenced by mixing of bands. For example, the top valence band of $\text{Si}_{12}\text{Ge}_{12}$ superlattice displays a partial Si and partial Ge character. Additionally, the contribution to the conduction bands is increasingly mixed near the Γ point, as can be seen from the ASFs of Si_6Ge_6 (row (f)) and Si_4Ge_4 (row (g)) superlattices. These results demonstrate that the Γ -character of the superlattice bands strongly depends on the composition. A continuous band mixing has been demonstrated both theoretically and experimentally for alloys [45]. Here, we illustrate the band mixing for layered heterostructured Si-Ge systems. The progression SF plots further suggest that a direct band gap system can thus be designed by tuning the Γ -character. Earlier studies have identified that Si_6Ge_6 superlattice shows nearly direct band gap [46] while Si_6Ge_4 has a direct band gap [16]. We analyze the band structures along a specific symmetry path, therefore, precise identification of the direct or indirect nature of the band gap is out of scope for the present study. Identifying a direct band gap configuration from two indirect band gap materials promises various practical benefits, however, can be challenging [16, 46]. Although designing such a system is not the objective of our current study, Fig. 7 shows how our ML assisted first-principles modeling approach can be employed to achieve such a goal.

Figure 7 illustrates how ASFs of strain symmetrized superlattices change due to the decrease of superlattice periods. The strain induced band splittings, mixing of bands, avoided crossings and changes of Γ -character are dominant characters displayed by the ASFs of short-period superlattices. These features provide a measure to differentiate the superlattice and the bulk bands. Quantifying these characters is critical both from the fundamental viewpoint and for materials design for target applications. Our approach establishes a direct relationship between atomic environments and these band characters for complex heterostructures.

COMPARISON OF FORWARD MODEL PREDICTIONS & DFT RESULTS

Figure 8 shows the forward model-predicted SFs for the strain-symmetrized configuration of a $\text{Si}_{28}\text{Ge}_{28}$ superlattice. This structure is outside the training set, which include $\text{Si}_{26}\text{Ge}_{26}$ superlattice as the largest superlattice. We show the supercell configuration in Fig. 8(a). The SFs are predicted along the $X - \Gamma - K - X$ path of the Brillouin zone of the reference cell, with similar k and E resolution as training data. Figure 8(b) shows total SFs and the bottom rows show the ASFs of atoms from four regions of interest: (c) inner Si, (d) interface Si, (e) interface Ge, and (f) inner Ge. The different regions are indi-

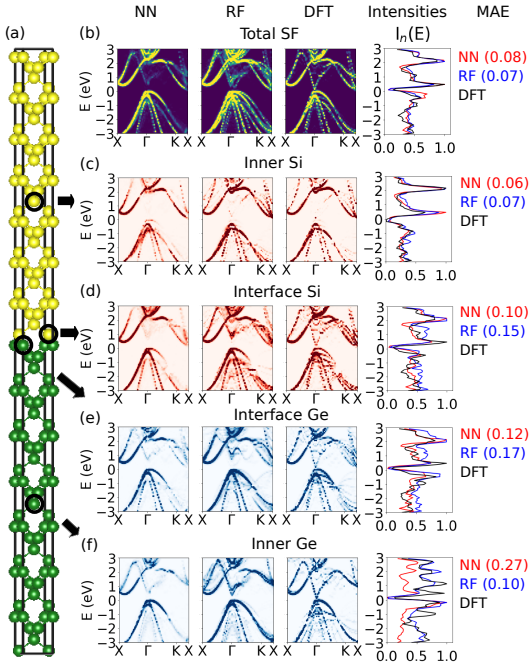


FIG. 8. **Total and atomically resolved spectral functions (SFs) of $\text{Si}_{28}\text{Ge}_{28}$ superlattice:** (a) Representative supercell configuration; (b) Total SF and ASFs of representative atoms in (c) inner Si region, (d) interface Si region, (e) interface Ge region, and (f) inner Ge region of the superlattice. NN and RF model predictions are shown in the first and second column of rows (b)-(f), respectively. Third column shows DFT results. Last column shows normalized intensities, $I_n(E)$, and MAEs between predicted and computed $I_n(E)$.

cated in the supercell with black circles (Fig. 8(a)). The total SFs are obtained by summing over the predicted ASFs of all atoms. The first and the second column of Fig. 8 show the ASFs predicted by the NN and the RF models, respectively. We compare the ML predictions with DFT results, shown in the third column and validate the predictions. We show the comparison between predicted and computed $I_n(E)$'s in the last column of Fig. 8 and report the MAEs.

The predicted total SFs display a mixture of Si-like and Ge-like characters, similar to DFT results, resulting in small MAEs (NN:0.08, RF:0.07). The presence of bulk-like character is similar to other large period superlattices. The predicted inner Si ASFs match with DFT results closely, yielding the smallest MAE 0.06 (Fig. 8(c)). In comparison, the DFT result of the inner Ge ASF exhibits splitting of the bulk-like bands, especially for the valence bands, near Γ point (Fig. 8(f)). The split band is less dispersive in the $\Gamma - K$ direction. The conduction band shows a small degree of splitting as well. These features are not captured in the NN prediction, resulting in a high MAE (0.27). Although the RF prediction cannot capture the splitting of the valence bands well, other

bulk-like features are relatively well predicted, resulting in a smaller MAE: 0.10.

Meanwhile, the interface Si ASFs are considerably different from their bulk counterparts (Fig. 8(d,e)). For example, a larger contribution of Ge-like bands can be noted in DFT results, compared to the inner Si ASF. However, it is interesting to note that the Si and Ge DFT interface ASF results are quite similar to each other. Both of them display a mixed character strongly influenced by strain. The interface ASFs exhibit significantly more band splitting compared to inner ASFs. The splitting is related to the varied strain environments near interface. The strain induced splittings are more pronounced for the valence bands. The split-off valence bands are comparatively flat near the Γ point. Both the NN and the RF model fail to capture the finer details, however, they predict an average character of the strain-split bands. Although the predicted and computed ASFs show differences, it is interesting to note that the total SFs exhibit similar patterns.

EFFECTS OF FERMI-LEVEL ALIGNMENT

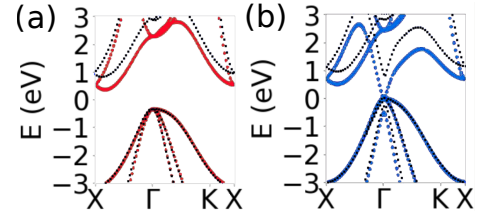


FIG. 9. **Band structures** of (a) bulk Si and bulk Ge obtained with PBE-GGA approach (solid lines). The dotted black lines represent results from GW calculation from literature [47].

It is known that the PBE-GGA approach fails to predict semiconductor band gaps accurately, as is particularly evident from Fig. 7(b). We show a comparison between PBE-GGA band structures and those obtained with GW calculations [47] (black dashed line) in Fig. 9. The valence bands obtained with the PBE-GGA approach match the GW results, however, the conduction bands are lowered resulting in an underestimated band gap. Such discrepancy has been discussed extensively [21, 22, 48–50]. Nevertheless, the PBE-GGA approach has been extensively used to predict the electron/hole transport properties of semiconductors, including the biaxial strain enhanced in-plane mobility in Si [51] and thermoelectric properties of Si [52, 53] and Si/Ge superlattices [15, 21–24, 54]. In previous publications, we compared the electronic transport properties [22] predicted using the PBE functionals and the Heyd-Scuseria-Ernzerhof [55]. Through a systematic analysis we illus-

trated the effectiveness of PBE-GGA approach to predict the relationship between lattice environment and electronic properties of semiconductor heterostructures. In this article, our objective is to develop a model for rapid prediction of this relationship. The computational cost of the alternative approaches such as using hybrid functionals [56, 57] or implementing GW calculations [47] prohibits the use of these approaches to analyze large structures, especially for data driven studies. Additionally, The prior studies provide necessary justification to use PBE-GGA approach to establish the model.

Here, we use data obtained with PBE-GGA approach to train ML models. We discuss the role of Fermi-level alignments on ML predictions. To obtain the results shown in main manuscript, we use one Fermi level alignment for the forward learning level, but different Fermi level alignments for the reverse learning model.

Forward Learning Approach: We assign the Fermi-level ($E = 0$ level) to be equal to the middle of the bandgap value, to obtain the total SF for each training configuration. The ASF energy bands are shifted by the corresponding amount. The forward learning model is trained with the resulting ASFs. We show the predicted ASFs and total SFs of test superlattices and heterostructures in Fig. 8 and Fig. 2 of main manuscript, respectively. As can be seen from the figures, both predicted energy bands and energy level alignments are in good agreement with the corresponding DFT results.

Different Fermi-level Alignments: We illustrate the change of ML predictions by varying alignments of training ASFs.

(Case I) Electronic band gap cannot be directly defined for the ASFs, to the best of our knowledge. We align the Fermi-level of each ASF of training superlattice to the respective mid-band-gap level. We task the trained ML model to predict ASF (or total SF in this case) for bulk Si systems. Bulk systems include atomic environments which is not present in the training structure that includes a mixture of both the materials. As we illustrate below, the Fermi-level alignment strongly affects the predictions in this case. Figure 10 shows the SFs of (a) relaxed and (b) strained Si. The systems are modeled with tetragonal supercells that include four Si atoms. The first and the second column show the SFs predicted by the NN and the RF models, respectively. The third column represents DFT results. We show the comparison between predicted and computed $I_n(E)$'s in the last column and report the MAEs. The mismatch between Fermi-levels is pronounced in the plot showing the normalized intensities for strain-symmetrized bulk Si. Interestingly, the predictions are in good agreement with the DFT SF results for bulk Si with in-plane strain.

(Case II) We align ASFs such that the zero-energy level of each ASF corresponds to the largest spectral weight at the Γ -point in the valence zone or valence band maximum (VBM). We retrain the model with VBM aligned-ASFs

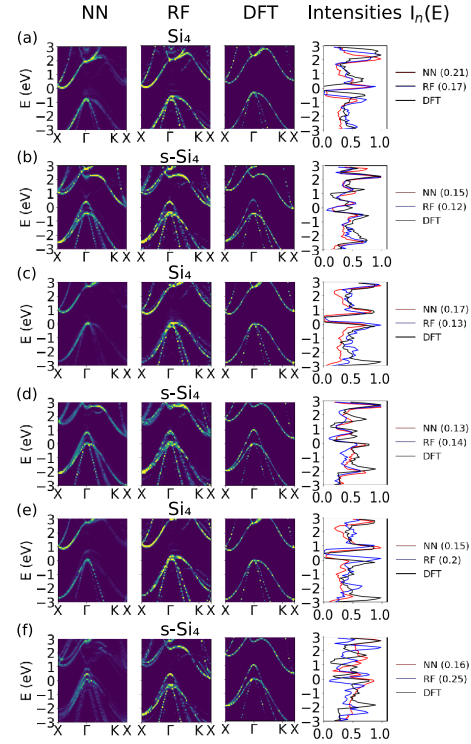


FIG. 10. Effect of Fermi-level alignment of SF on ML performance: (a-b) ASFs with Fermi-level aligned at the mid gap level. Predicted SFs for (a) relaxed bulk Si and (b) bulk Si in tensile strain due to Ge substrate. ASFs with Fermi-level aligned at VBM, independently for each ASF: Predicted SFs for (c) relaxed and (d) strained bulk Si. ASFs with Fermi-level aligned at VBM, independently for each total SF: Predicted SFs for (e) relaxed and (f) strained bulk Si.

and task the model to predict ASFs for the bulk systems. The predictions are shown for relaxed and strained bulk Si systems in Fig. 10(c,d). In this case, both the peak intensities and the energy alignments are reproduced with a good agreement with DFT results.

(Case III) We align the total SF of each training superlattices such that the zero-energy level is set to the largest spectral weight at the Γ -point in the valence zone or VBM. The energy bands of ASFs are shifted by the corresponding amount. The ML predictions for the bulk systems are shown in Fig. 10(e,f). The NN predicted relaxed Si bands are better aligned than RF, however the spectral weights are diminished for the NN predictions. The predictions for both relaxed and strained Si are worse than the ones reported for case (II).

As can be observed from above discussion, the ML predictions vary in an unpredictable manner depending on the energy level alignments of training ASFs. To generalize and diversify the training set for the reverse approach, we consider 13 Fermi level alignments in incremental steps in the range from +0.5 eV to -0.5 eV from the mid-gap energy level. The various alignments cor-

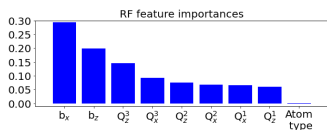


FIG. 11. RF feature importance

respond to different electron doping in ARPES experiments.

Reverse Learning Approach: We test the CNN model to predict the descriptors of bulk Si systems when the SF images are provided as input. We use two categories of test images: the DFT predicted SFs of relaxed and strained bulk Si and a spectra obtained from ARPES experiment. In practice, only the valence bands may be available in the ARPES experimental images. To adapt to such constrains, we train the reverse ML model with the energy levels of DFT results below the VBM level. In other words, the ASFs are aligned individually such that the zero-energy level corresponds to the largest spectral weight at the Γ -point in the valence zone. As discussed above, the band gap is not directly defined for the ASF, so the shift in the Fermi level is ambiguous. This provides a way to expand the training data set by applying various amount of shifts. The CNN model is then trained on the corresponding ASFs. The CNN approach has shown high level of efficiency with image data sets. We expect the CNN model to capture unique patterns in the ASF rather than the shift associated with the different Fermi-level alignments.

TRAINING FORWARD AND REVERSE ML MODELS

The feature importance for RF model is shown in Fig. 11. As shown in the figure, b_x has the highest importance as it is the measure of in-plane strain that induces band splittings. b_z is the next most important feature, that is responsible for internal interatomic distances due to different atom types in the configuration. Interestingly, the higher order parameters are of the higher importance, we attribute that to their long range sensitivity to the presence of material interfaces. Importance of the atom type seems diminished, which can be explained by the fact that only two atomic types are considered. The other features can distinguish the atomic environments indirectly. This, however, may change when many atomic species are present in the training configurations.

The learning curves during the training of forward NN and reverse CNN model are shown in Fig. 12 and Fig. 13, respectively. As the figure shows MAEs change as we change the number of epochs of the model. We select

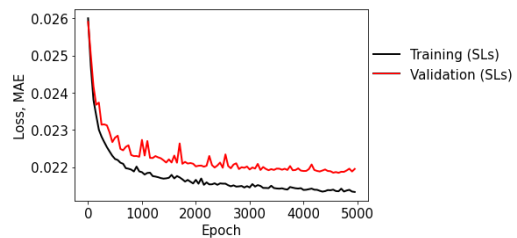


FIG. 12. Learning curves for NN.

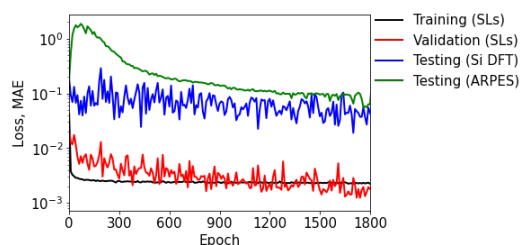


FIG. 13. Learning curves for CNN.

the epoch with lowest validation set MAE (red curves). In this article, we present the results obtained with epoch 4700 and 1750 for the forward NN and CNN model, respectively. However, choice of these numbers is arbitrary.

TEST OF REVERSE LEARNING MODEL

Heterostructure: We test the performance of the reverse learning model on the multilayer heterostructure, $\text{Si}_{24}\text{Ge}_{15}\text{Si}_9\text{Ge}_6\text{Si}_3\text{Ge}_3$. The chosen configuration is strain-symmetrized. We show the CNN-predicted descriptors for all atoms of the heterostructure in Fig. 14. Figure 4 of main manuscript shows the model performance on a strained configuration of the same heterostructure. The prediction error is higher for the strain-symmetrized configuration. We speculate that the higher error arises because the number of strain-symmetrized configurations is small in the training set compared to strained configurations.

Bulk systems: We consider bulk Si and bulk Ge models grown on $\text{Si}_{1-x}\text{Ge}_x$ substrate with varied concentrations, x , that induces four different strains: 0.00%, 0.59%, 1.16%, 1.73%. We refer to the strained Si and Ge as s-Si and s-Ge, respectively. It is important to note that the training set only includes superlattices and do not include any information about pristine bulk material. The bulk SFs are provided to the combined model as input. We show the CNN-predicted descriptors in Table 6. The CNN model predicts atom type= 1 (or type= 2) for all Si (or Ge) test structures. The model is able to perceive the absence of Ge (or Si), even though all ASF training

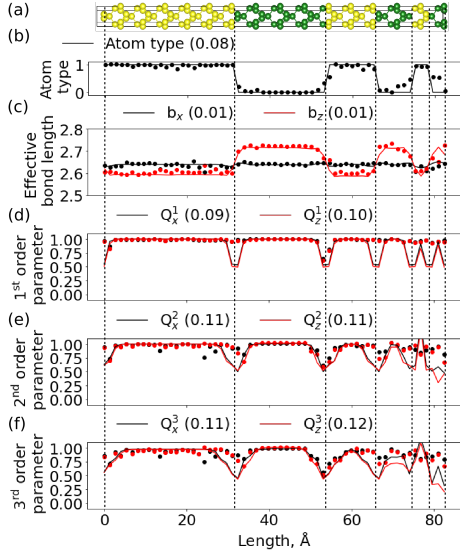


FIG. 14. CNN predicted atomic environment descriptors of strain-symmetrized $\text{Si}_{24}\text{Ge}_{15}\text{Si}_9\text{Ge}_6\text{Si}_3\text{Ge}_3$ heterostructure: (a) Supercell configuration; Predicted (b) atom type, (c) effective bond length and (d-f) spatially resolved order parameters, Q_i^{order} where $i = (x, z)$ and $order = 1, 2, 3$. MAEs between predicted (circles) and calculated features (solid lines) are shown within parentheses, next to legends.

data include Ge (or Si) signatures. The identical b_x and b_z are also accurately predicted for relaxed bulk Si and Ge. The applied in-plane strains directly affect the bond lengths. b_x 's increase with higher in-plane strain. To keep the volume constant, b_z decreases. It is remarkable that the predicted order parameters are all close to the bulk values (~ 1), even in highly strained systems. This result indicates that order parameters are highly effective in distinguishing mixed environments from pristine ones. Figure 5 in main article shows the comparison between $I_n(E)$, computed from the output of the combined forward-reverse model and DFT data for two Si systems. We find a good agreement between predicted and computed normalized intensities for all systems.

TABLE 6. Computed and Predicted Si & Ge Descriptors

Test image	type	b_x	b_z	Q_x^1	Q_z^1	Q_x^2	Q_z^2	Q_x^3	Q_z^3
Si	DFT	1.00	2.58	2.58	1.00	1.00	1.00	1.00	1.00
	CNN	0.99	2.61	2.61	1.00	1.00	1.00	0.99	1.00
s-Si [1] (0.59%)	DFT	1.00	2.62	2.60	1.00	1.00	1.00	1.00	1.00
	CNN	1.00	2.61	2.61	1.00	1.00	1.00	0.97	0.97
s-Si [2] (1.16%)	DFT	1.00	2.61	2.57	1.00	1.00	1.00	0.97	0.97
	CNN	1.00	2.64	2.60	1.00	1.00	1.00	1.01	0.97
s-Si [3] (1.73%)	DFT	1.00	2.63	2.57	1.00	1.00	1.00	1.00	1.00
	CNN	1.00	2.64	2.59	0.99	1.00	1.00	1.00	0.98
Ge	DFT	0.00	2.73	2.73	1.00	1.00	1.00	1.00	1.00
	CNN	0.01	2.66	2.70	1.00	1.00	1.00	0.99	1.00
s-Ge [1] (0.00%)	DFT	0.00	2.60	2.81	1.00	1.00	1.00	1.00	1.00
	CNN	0.01	2.56	2.77	1.00	1.00	1.00	0.97	0.99
s-Ge [2] (0.59%)	DFT	0.00	2.61	2.80	1.00	1.00	1.00	1.00	1.00
	CNN	0.01	2.58	2.76	1.00	1.00	1.00	0.97	0.99
s-Ge [3] (1.16%)	DFT	0.00	2.62	2.80	1.00	1.00	1.00	1.00	1.00
	CNN	0.01	2.59	2.76	1.00	1.00	1.00	0.98	0.99
s-Ge [4] (1.73%)	DFT	0.00	2.63	2.79	1.00	1.00	1.00	1.00	1.00
	CNN	0.01	2.60	2.75	1.00	1.00	1.00	0.98	0.99